ISTITUTO NAZIONALE DI FISICA NUCLEARE

Sezione di Milano

Titolo

ASTAROTH Cryogenic Chamber Design and Test Report

Autori
Simone Coelli – INFN Milano, Davide D'Angelo, Univ. Milano
Mauro Monti INFN Milano, Arsenio Palmisano INFN LASA,
Maurizio Todero INFN LASA, Andrea Zani INFN Milano

Abstract

In order to validate the design of the cryogenic chamber of the ASTAROTH experiment, finite element analysis and mechanical material characterisation
tests were carried out under cryogenic conditions.
This document summarises the results of the analyses and tests conducted jointly by the INFN Milano Design and Mechanical Workshop Service and at the INFN LASA Laboratory.

Istituto Nazionale di Fisica Nucleare

Sezione di Milano

ASTAROTH Project Document	Institute Document No.	Created: 06/10/2022	Page: 1 of 56
	INFN-MI-AST-22.01.001	Modified : 31/01/2025	Rev. No. 1

ASTAROTH Cryogenic Chamber
Design and Test Report

Abstract

In order to validate the design of the cryogenic chamber of the ASTAROTH experiment, finite element analysis and mechanical material characterisation tests were carried out under cryogenic conditions.
This document summarises the results of the analyses and tests conducted jointly by the INFN Milano Design and Mechanical Workshop Service and at the INFN LASA Laboratory.

Prepared by:	Checked by:	Approved by:
Mauro Monti - INFN Milano **Simone Coelli - INFN Milano** **Andrea Zani - INFN Milano** **Maurizio Todero - INFN LASA** **Arsenio Palmisano - INFN LASA**	**Simone Coelli - INFN Milano**	**Davide D'Angelo - INFN Milano** **Andrea Zani - INFN Milano**

History of Changes

Rev. No.	Date	Pages	Description of changes
DRAFT	06/10/2022		
DRAFT.1	05/12/2022		Added section 4
DRAFT.2	29/01/2022		Added section 1,2,3 – cleaned section 4
DRAFT.3	07/06/2024		Added subsections 4.xx about room test temperatures. Corrected Section 4.yy on true stress/strain
DRAFT.4	09/07/2024		Updated section 5 (FEA), and added buckling analysis subchapter 5.3
DRAFT.5	23/07/2024		Added section on bending tests (now, section 5); general text review; added some references in sections 1 and 2; added text in Conclusions section. FEA is now section 6.
REV.0	29/08/2024		Added figure 3.1 and reference to annex drawings, cleaned and finalized text. Resolved all remaining comments
REV.1	31/01/2025		Added acknowledgements, revision of sentences.

Table of Contents

1   Introduction

The search for Dark Matter (DM) has still to provide definitively positive results, despite the continued construction of experiments with increasing target mass and exploiting different techniques and signatures. Since over twenty years, the DAMA experiment at the underground Gran Sasso National Laboratory (LNGS) is observing an annual modulation of the interaction rate in arrays of NaI(Tl) crystals [1]. Although this modulation satisfies all the conditions to be interpreted as DM interaction, a model independent verification has never been possible so far. The DAMA result and its interpretation has been challenged many times since the initial claim, proposing numerous alternative hypotheses related to Earth-bound phenomena. However, as of today, none of these has been ultimately able to explain the observation. On the other hand, while several other experiments around the world fail to observe a compatible signal [2, 3, 4], their result cannot be compared with DAMA's claim in a straightforward manner, due to the use of different targets/techniques. Present generation experiments based on NaI(Tl) crystals, read-out by PhotoMultiplier Tubes (PMTs) [5, 6, 7] have not yet managed to obtain a low enough radiopurity of the materials to be fully competitive with DAMA; however, initial results do not shown evidence of modulation, as well [6, 7]. Achieving a next-generation detector based on NaI(Tl) with a sensitivity comparable with, or higher than, DAMA is mandatory, to perform a model-independent test of this long-standing claim and in case a dark matter induced annual modulation is present, to shed light on its nature.

2   The ASTAROTH experiment

The ASTAROTH project is a novel proposal to overcome the described limitations, thanks to the adoption of Silicon PhotoMultipliers (SiPM) for the read-out of scintillation light from NaI(Tl) crystals [8, 9]. Such a detector is therefore cryogenic, as the high dark count of SiPM at room temperature makes them unsuitable for low energy applications. Liquid argon (LAr) is the natural solution to obtain a low-temperature environment and at the same time implement an active veto around the detectors. The idea is that, by surrounding the crystals with a volume of LAr, one can perform active rejection on some of the most dangerous backgrounds for the experiment. We have designed a dedicated cooling system with the goal of bringing up to two crystals, coupled with SiPM arrays, down to a chosen operative temperature in the [87 - 150] K range and safely back to room temperature. The cool-down and warm-up phases must be slow and controlled, in order to ensure the survival of the crystals and their cases at all times and across several cycles. In particular: (1) the temporal temperature gradient must be limited to < 20 K/h; (2) the spatial temperature gradient (within each crystal) must remain < 1 K. Moreover, the temperature stability during data taking must be ensured within 0.1 K, in order to guarantee the steady response of the crystal and of the electronics, in the prospect of a subsequent run for dark matter investigation.

For these reasons, a dedicated cryogenic chamber has been designed to house and cool down safely up to two crystals. The focus of this note is to describe in detail the reasoning behind the design of the chamber: its technical description will be presented in Section 3; Sections 4 and 5 describe the tensile test for the Copper material characterization and bending test for the qualification of the brazed samples. In Section 6 the Finite Element Analysis (FEA) work is described and in particular the use of material properties information from the mechanical tests as input to perform a full set of thermo-mechanical simulations to validate the behaviour of the chamber under the stress from pressure (internal vacuum or low pressure conditions) and moreover from the temperature cycling. The results of the simulations are fundamental for the mechanical verification of the chamber under any condition foreseen.

3 Technical description of the Copper-Stainless Steel cryogenic chamber

The main driver of the Copper-Stainless Steel Cryogenic Chamber (from now on, cryo-chamber) is the need to cool-down and warm-up the NaI(Tl) crystals in a slow and controlled way, in order to ensure the survival of the crystals themselves and of their quartz cases, at all times and across several cycles.

The design is based on the hypothesis that the natural cooling power provided by the LAr may be exploited adequately to keep stable conditions in the main detector volume. The idea is that cooling can be achieved efficiently by immersing the chamber in a bulk of cryogenic liquid, and then raising/stabilising the temperature through an inner heating element. **Figure 3-1** below shows an extract of the chamber drawings (side view and section). The design is described in detail in the following.
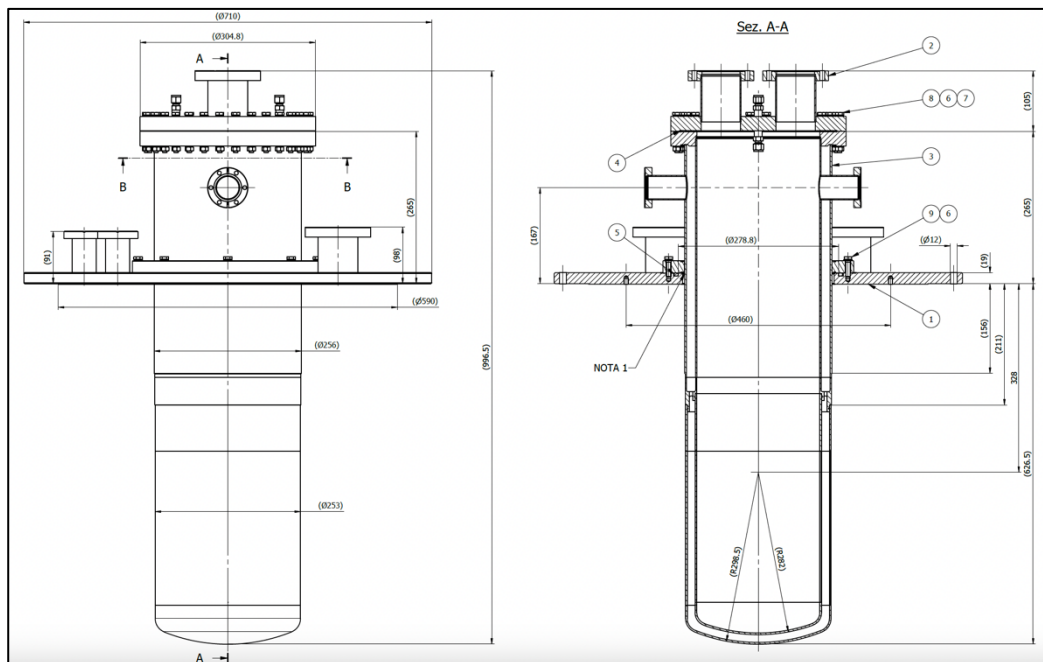

Figure 3-1: extract of the overall drawing of the chamber, showing most dimensions and the components.

The chamber consists of a main volume of OFHC Copper and 316L Stainless-Steel chimney. The chimney can be connected to the main flange of an external dewar, 600 mm inner diameter, 1000 mm height. The copper chamber is dual-walled and vacuum-insulated. The two walls are 3 mm thick and are connected by a specially designed stainless-steel thermal bridge. The cavity is 13.5 mm wide, and the outer copper wall is 253 mm in diameter. The chimney is also dual-walled, vacuum-insulated (2 mm thick stainless-steel walls) and it forms one volume with the copper chamber inner wall cavity: several holes on the thermal bridge (16 × ø 5.5 mm) allow pulling vacuum in both volumes through a single port on the side of the chimney.

The liquid cryogenic bath in the external dewar provides cooling power, diffusing on the inner copper wall mainly by conduction through the SS bridge. Radiation through the two copper walls has been estimated as negligible. This allows slow cooling the inner volume (and the crystals) down to 87 K. An adjustable power heater on the inner chamber wall is used to raise the temperature in a controlled way up to 150 K and keep it stable. Low pressure Helium gas

(100-200 mbar absolute) fills the inner volume, serving as heat-transfer medium to the crystals, and providing the necessary thermal inertia.

Few thin disks are placed along the chimney, with external radius slightly smaller than the chimney inner dimension, and with holes optimized for cable routing. Three to four stainless-steel disks are foreseen on the higher part of the chimney, whereas one final copper disks will be placed 10 cm below the heating element. These components are in place to obtain stratification of the gas within the chimney, thus minimizing the heat exchange via convection with the top part of the chimney. The disks and the crystals are all supported via a structure relying on bar that are made in G10, i.e., a thermally insulating material: this minimizes the conduction from the top of the chimney. It should be noted that G10, i.e., glass-fiber, is radio-dirty; therefore, for the actual physics run, it should be substituted with PEEK, which is equally insulating but much radio-cleaner and more expensive.

In general, this design aims then at exploiting conduction through the thermal bridge as the main process of heat exchange between the crystals and the outer tank.

4   Tensile tests for copper characterization

As part of the copper-stainless steel cryogenic chamber characterization, a testing campaign has been put in place to measure the mechanical properties of the copper employed for the chamber construction. Indeed, it is difficult to obtain from literature a consistent picture of such properties at low temperature, given the fact that they are strongly dependent on the machining process (history) and the microscopic properties of the material (purity, grain dimension).

The final goal of the project is to exploit, as cryogen and scintillator, liquid argon (LAr), which is liquid at 87 K. However, the initial R&D tests will be carried out with liquid nitrogen (LN2), which is liquid at 77 K. There is no evidence in literature for significant changes in the mechanical properties of copper and stainless steel across this limited temperature range, and indeed most existing measurements are done at 77 K. For this reason, the characterization of the materials in this project has been carried out at LN2 temperature.

4.1   Introduction

LASA (*Laboratorio Acceleratori e Superconduttività Applicata*, Laboratory for accelerators and applied superconductivity) is a facility of University of Milan and INFN Milan with availability of an INSTRON machine, to perform tensile characterization of materials from room temperature down to 4 K, using liquid Helium. It allows performing measurements at 77 K, using liquid nitrogen (see **Section 4.5**).

The ASTAROTH collaboration has procured four samples of the same copper used for the construction of the cryogenic chamber (C110/642). The design of these samples is to some degree customized, however it has been developed in order to adhere as much as possible to European regulation EN 10002 – part 1. The samples are 3 mm thick. On the other hand, the INSTRON machine usually accepts circular samples, therefore two holding clamps were also designed, with the collaboration of the machine operators and the production company. These allow interfacing the machine connection points with the two ends of the copper samples (detailed design of the samples is reported in **Section 4.4**).

4.2   Equipment and test procedure

The available material for the test, as anticipated in the Introduction, is:
- Four copper samples (C110/642), cold-drawn with an unknown degree of hardening, with rectangular section.

- Two holding clamps, made of two connecting pieces each, in stainless steel AISI 316L.

The instrumentation available at LASA is listed below:
- INSTRON machine for tensile test with load cell with reach up to ± 200 kN.
- Cabinet with four roughing pump and a turbomolecular pump, along with user interface to regulate pumping speed and cooling cycle (temperature setting, regulation and read-out, pressure read-out).
- Custom cryostat for the execution of the cryogenic tensile tests, by Oxford Instruments.
- Dedicated software for the remote control of the machine and the execution of the tests, by Merlin.
- Two cryogenic axial strain gauges, called StrainGauge A and StrainGauge B.
- General purpose instrumentation for sample measurement and setup (dis-)assembly.

Each sample undergoes a "qualification test" in two phases; whenever possible, European regulation EN 10002 – part 1 has been followed.
Phase 1:
- Application of cryogenic axial static strain gauge on the sample.
- Sample installed in the cryostat and fully immersed in liquid nitrogen (77K). Cool-down and stabilization at around 77.0±0.5 K take around five hours.
- Measurement of Young's modulus, Yield Strength Rs and load Rp0.2, with crossbeam movement set in "stroke control" mode.
- Warm-up of the cryostat overnight.
Phase 2:
- Removal of the strain gauge, second cool-down cycle of the sample (77K).
- Measurement of sample Ultimate Strength Rm with crossbeam movement set in "stroke control" mode.
- Warm-up of the cryostat overnight.

The correct operation of the INSTRON machine, of the cooling and pumping system and of the strain gauges has been fully verified before the testing campaign, with the use of a standard cylindrical stainless-steel sample.

4.3　　Technical specifications of the Instrumentation

4.3.1　　*Fundamental parameters and relations among parameters*

F = tensile force (N)
A = area of the sample section before the test (mm^2)
l = "useful stretch" or distance between the strain gauge knives (mm)
λ = elongation or displacement of the strain gauge knives (mm)
E = Young's modulus of the material under test (N/mm^2)
ε = strain (mm/mm)
σ = internal stress generated by F (N/mm^2)

Fundamental relations:

$$\lambda = \frac{F \cdot l}{E \cdot A} \; ; \qquad \varepsilon = \frac{\lambda}{l} = \frac{F}{E \cdot A} \; ; \qquad \sigma = E \cdot \varepsilon.$$

(4.1)

It should be noted that the relations above, especially the last one, refer to what is usually defined as *engineering stress/strain*. The third relation above and the related curve, in

particular, do not take into account the effect of shrinking of the sample cross section during the tensile test. In order to take this into account, the values of engineering stress/strain should be corrected, to produce the so-called *true stress/strain* relation.

$$\sigma_t = \sigma_{eng}(1 + \varepsilon_{eng}); \qquad \varepsilon_t = ln(1 + \varepsilon_{eng})$$

(4.2)

These relations are generally assumed to be valid in a range between twice the value of Rp0.2 and the necking value. Beyond this limit, no relation can be used a priori to relate true and engineering stress/strain, and the instantaneous sample cross section must be measured.

4.3.2   INSTRON Machine

Specifications of machine components:
Load Cells:
- Three available: ±0.1 kN; ±10 kN; ±200 kN;
- Precision: max value between ±0.5% of the read-out value and ±0.1% of full scale.
- Given the available literature values of Rm for copper (around 350 MPa) and an average value of the sample area of 36 mm², the ±200 kN is selected for the test.

Crossbeam:
- Displacement speed in range: [0.002; 500] mm/min.
- Precision: ±0.1% of displacement speed, at constant load.

4.3.3   Strain Gauges

As mentioned in the Introduction, two gauges "A" and "B" are available. With reference to section 4.3.1:
- l = 10 mm;
- max λ = 1 mm; (full scale is 10% of l);
- linearity = 0.002 mm.

4.4   Precision measurement of the copper samples

Below the technical drawing of the copper samples is reported, along with the actual measurements of the real samples.
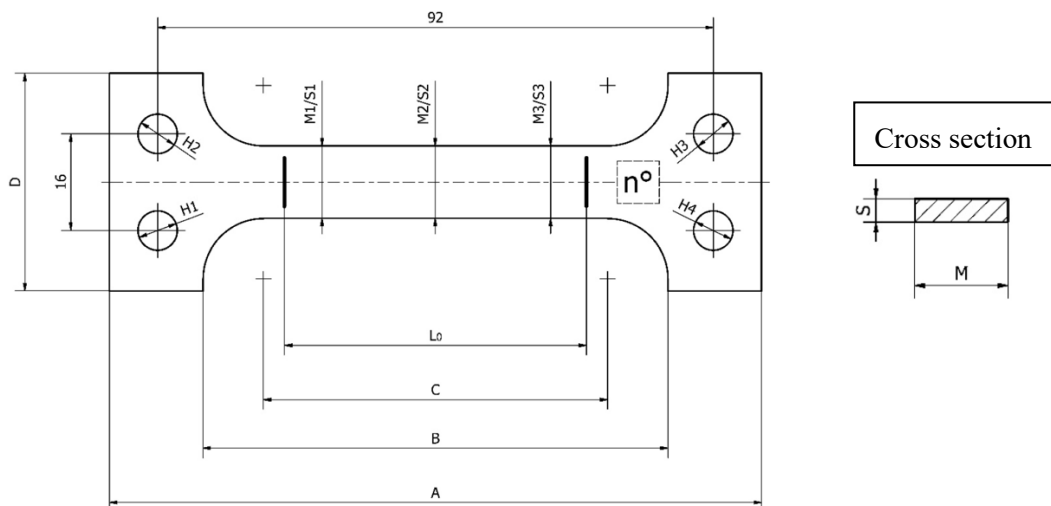

Figure 4-1: 2D drawings of the copper samples, with highlighted dimensions detailed in Table 4-2

#	Resisting section [mm^2]
1	35.1
2	35.1
3	36.0
4	34.8

Table 4-1: Measured resisting section of the four copper samples

n°	Lunghezza [mm]					Sezione [mm]						Fori [mm]				
	A	B	C	D	*L0	M1	M2	M3	S1	S2	S3	H1	H2	H3	H4	Hm
1	108,7	77	55	36,1	48,9	12,1	12,1	12,1	2,9	2,9	2,9	6,6	6,6	6,6	6,6	6,6
2	108,3	77,1	54,7	36,1	48,6	12,1	12,1	12,1	2,9	2,9	2,9	6,5	6,5	6,5	6,5	6,5
3	108,1	77,2	52,3	36,1	46,3	12	12	12	3	3	3	6,5	6,5	6,5	6,5	6,5
4	108	77,2	52,8	36	46,8	12	12	12	2,9	2,9	2,9	6,7	6,7	6,7	6,7	6,7

Table 4-2: table of dimensions of the four copper samples, as defined in Figure 4-1

$*L0 = C - M/2$ $Hm = (H1+H2+H3+H4)/4$

$Mm = (M1+M2+M3)/3$ $Sm = (S1+S2+S3)/3$ Resisting Section $= Sm \cdot Mm$

It should be noted that all samples are affected by a construction defect: the minimal section is at the junction between the radius of the head and the straight part of the section. This is expected to cause rupture at the limit (or beyond) the gage length L_0.

4.5 Test preparation procedure

The sample is inserted with the appropriate clamps (already tightened) inside a centring cage connected to the titanium tensile shaft (**Figure 4-2**). Two temperature sensors (see below for details) are then attached to the cage: T2 at the upper end and T3 at the lower end to ensure proper temperature monitoring (**Figure 4-2, right**).

The cryogenic strain gauge is attached to the centre of the sample and fixed by small stainless steel springs, to ensure it will not slide against the sample during the traction. The strain gauge has a fixed leg and a moving leg; during the traction, the moving leg will precisely track the axial elongation. Strain gauge "A" was used for this first test.

In addition, given the different coefficients of thermal expansion (CTE) of the materials (Cu sample and stainless-steel centring cage), in order to avoid stresses generated by mechanical interference, 0.2 mm is left between the centring cage and the clamps.
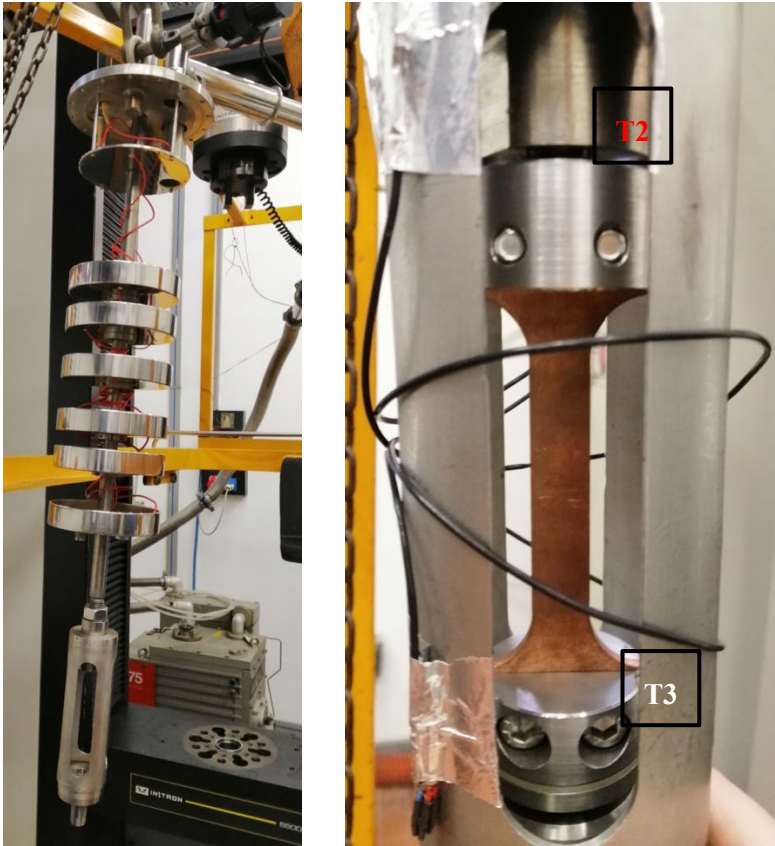
Figure 4-2: Left: Shaft to be inserted in the dedicated cryostat for cryogenic testing (it can be used independently for room temperature tests). In the background, the load cell and the crossbeam of the Instron machine are visible. Right: detail of one sample inserted in the centering cage, with installed temperature sensors T2 and T3.

The shaft top and mid sections are equipped with multiple shields (disks) to avoid convection of the cold gas inside the cryostat, and therefore stratification and stable temperature at the bottom, where the centring cage and the sample are sitting. Multiple ports on the top section serve gas circulation as well as extraction of signals from temperature sensors and strain gauge. For these tests, the shaft with the installed sample is inserted in the dedicated cryostat that will be connected to the INSTRON Machine. The connection is made through the load cell (connected to the inner shaft) and through the crossbeam. Temperature monitoring is performed through three RhFe sensors, called T1, T2, and T3, respectively.
- T1 and T2 were calibrated to 30 calibration points (more accurate).
- T3 was calibrated to 3 calibration points.
While T2 and T3 are located close to the specimen, as mentioned above, T1 is located close to the heat exchanger, which regulates the inlet temperature of the cryogenic liquid, allowing a temperature stability of ±0.5 K.
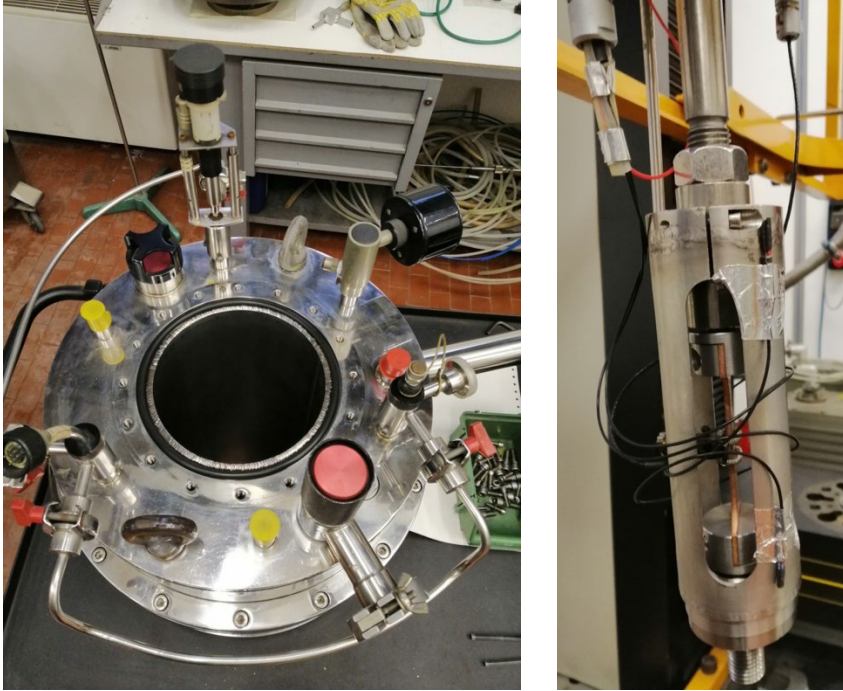
Figure 4-3 Left: top view of the cryostat that hosts the shaft. Ports for gas/liquid handling, and safety elements are visible. Right: sample installed and instrumented with the strain gauge. The springs used to maintain the gauge in position are visible.

It should be noted that the centring cage helps redistributing the weight (load) of the full shaft around the sample, avoiding risks of compression. However, the first test demonstrated that the holding clamps were still showing some small interference with the cage. Therefore, after careful testing, it was decided to remove the cage for samples 2, 3 and 4.

4.6   Test concept

The series of test that follow are made up of three separate tasks

1. Cooling cycle of samples: this is repeated at least twice for each sample, one for the study of yield strength and the other for the verification of the Ultimate Stress. This cooling cycle was first tested with a test piece, before moving on to the copper samples.
2. Yield strength test: increase strain beyond the proportionality (elastic) limit; calculate Young's modulus (E) as the slope of the linear fit of stress-vs-strain data; translate the same fit horizontally to reach 0.2% strain and find back on the data curve the corresponding value of the Offset Yield Strength (Rp0.2).
3. Ultimate strength test: determine the Ultimate Strength (Rs) value during the test; after the sample is brought back to room temperature, measure the increase of the gage length L0 and derive the percentage elongation A%.

4.7   Cryogenic Sample 1

The test of the first sample exploited strain gauge "A", which experienced an issue during the test, making it not useful for the determination of E. However, completing the full procedure allowed drafting a few lessons learned.

4.7.1   *Yield Strength – configuration and lesson learned*

Cooling cycle details.

- Cool-down time: **370 minutes**.
- Cooling rate: **0.57 K/min**.

- Target temperature: **77 K**.
- Operating pressure: **0.6 bar(a)**.

Due to the mentioned issue with strain gauge "A", the test cannot be used for further analysis. A dedicated verification of the two strain gauges showed that gauge "A" had developed an issue in the reported elongation value returned by instrument. Following samples were tested with gauge "B", which instead demonstrates stability of performance over repeated cycles.

4.7.2 *Ultimate strength – configuration and lessons learned*

Cooling cycle details.
- Cool-down time: **310 minutes**.
- Cooling rate: **0.69 K/min**.
- Target temperature: **77 K**.
- Operating pressure: **0.6 bar(a)**.
- Pre-load on sample: **100 N**.

The test was conducted by controlling the displacement speed of the crossbeam, in the range (0.2 – 0.5 mm/min). The resulting plot is reported below in **Figure 4-4**.
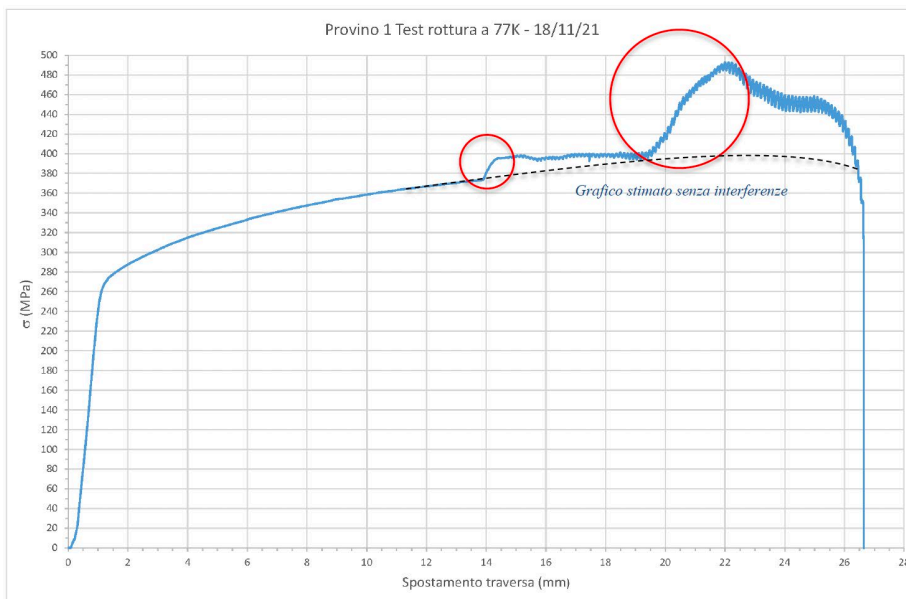

Figure 4-4: Stress vs crossbeam displacement for sample 1. Details in text

The plot shows an unexpected behaviour in the range between 14 mm elongation and breakdown. This represents the **first lesson learned**. Upon warming up the sample and opening the set-up, it was noted that the clamps holding the sample have a tiny interference with the cage surrounding the sample itself. Friction between the cage and the bottom clamp during the test caused the strange behaviour shown in the plot. **For later tests, it was decided to remove the cage**, which is not mandatory in the operation of the machine.

The visual exam of the sample shows that the breakdown occurred on the edge of the gage length. This prompted a new measurement of the width of two samples, demonstrating that the region where the head radius and the straight central body of the sample connect is slightly thinner than the body itself. This imperfection prompts the breaking in the area at the edge of the gage length. This is the **second lesson learned**. Below in **Table 4-3**, one can find the data on the width of samples 3 and 4 in various points of their body.

Sample #3	M (mm)		Sample #4	M (mm)
M1	11.82		M1	11.84
M2	11.98		M2	11.98
M3	11.98		M3	11.95
M4	11.83		M4	11.78

Table 4-3: Summary of measurements of section along different point of samples3 and 4. The drawing on the side shows where the measurements were taken.
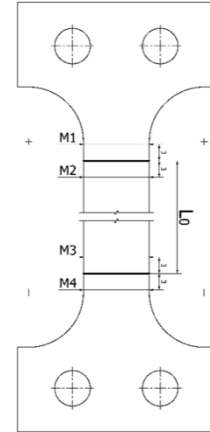
Finally, the **third lesson learned** is that closed visual exam reveals **small deformations in the holes on the heads** of the samples. This is expected, and it is due to shear stress induced by the friction between the sample itself and the holding clamp. This effect will be probably emphasized with softer copper.

The breakdown of the sample happened just within the edges of the gage length, with a final measured **elongation ΔL = 22.8 mm**. This translates in a **% elongation A = 46.5%**.

Below, **Figure 4-5** shows the broken sample and the details of the deformation induced on the head by the holding clamp.
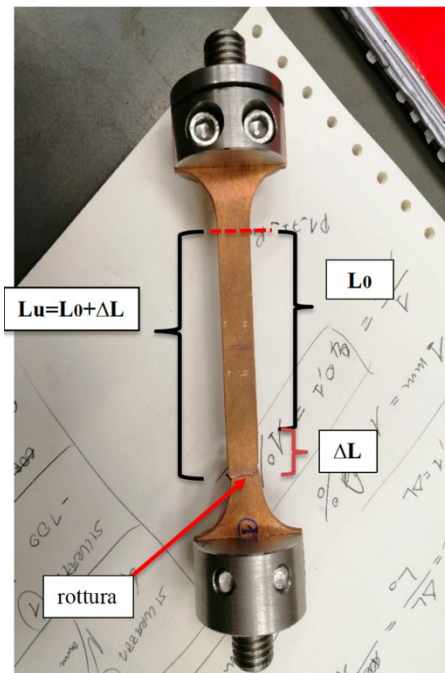
Figure 4-5 Left: broken sample with indication of elongation. Right: detail of the head where the effect of the clamping can be seen. The tiny deformation of the holes is barely visible in this case

4.8   Cryogenic Sample 2

4.8.1   Yield Strength test

This test was successful, and it was the first one to lack the centring cage around the sample. Cooling cycle details.

- Cool-down time: **290 minutes**.
- Cooling rate: **0.73 K/min**.

- Target temperature: **77 K**.
- Operating pressure: **0.6 bar(a)**.
- Pre-load on sample: **100 N**.
- Cross-beam speed: **0.2 mm/min**.

The result of the test is reported in **Figure 4-6**. The value of the Young Modulus (E) is calculated starting from the (X,Y) values of points P1, P2.
$E = \sigma / \varepsilon = 148.3$ GPa;
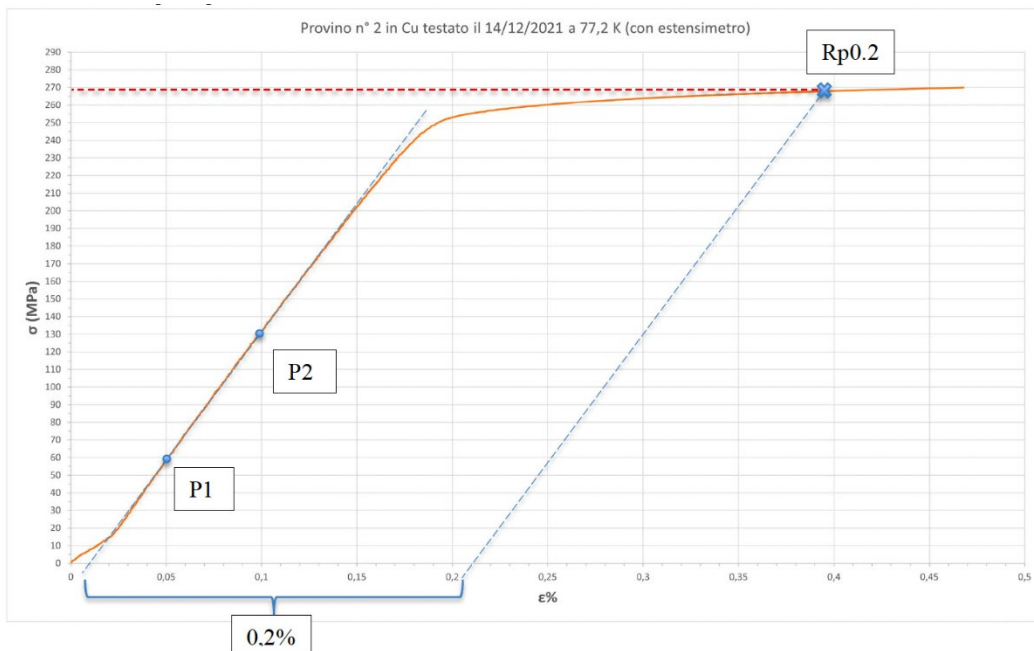Yield strength = **220 MPa**;
Rp0.2 = 268 MPa.

Figure 4-6: Stress vs strain for sample 2, with details of how E and Rp02 are calculated

4.8.2 *Ultimate Stress test*

Cooling cycle details.
- Cool-down time: **300 minutes**.
- Cooling rate: **0.71 K/min**.
- Target temperature: **77 K**.
- Operating pressure: **0.6 bar(a)**.
- Pre-load on sample: **100 N**.

The result of the test is reported in **Figure 4-7**. The sample again broke down within – but close to the edge of – the gage length.
Ultimate stress **Rs = 384 MPa** ;
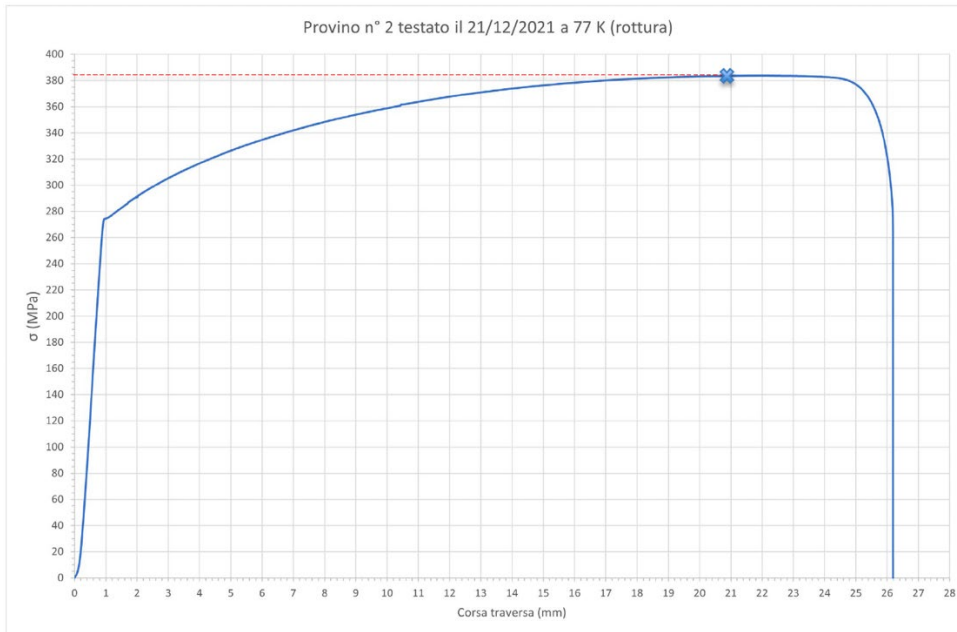Elongation **ΔL = 21.9 mm** (L0 = 48.6 mm);
% elongation **A% = 45%**.

Figure 4-7: stress vs crossbeam displacement for sample 2. The dashed line eases identification of Ultimate Stress value

4.9 Baking of samples 3 and 4

A portion of the cryogenic chamber is characterized by a brazing connecting copper and stainless steel. The brazed connections (section view) will be shown in **Figure 6-2**, later. This copper tested samples. Four brazed samples were also produced along with the main component of the cryogenic chamber therefore is baked during the brazing procedure and in very different mechanical conditions, with respect to the previously, in order to perform bending tests in LN2 of the connection (see **Section 5**). The producing company has released the details of the baking cycle performed in a vacuum oven on the brazed components.

Before testing samples 3 and 4, it was therefore decided to bake them in a small oven made available by the University of Milan. This oven is characterized by a small chamber, 10x8.5x19 cm in dimensions, for a ~1.6 litres volume; it is operated with pure Argon flushing. Before baking the samples, a test run was performed, to understand the inertia of the system. The actual baking cycle was then performed, trying to reproduce as faithfully as possible the cycle made by the company. Before the start of the heating phase, the oven was vacuum pumped for 10 minutes. Four vacuum cycles were then run, alternatively filling the oven with grade 6.0 argon, and then emptying it with a primary vacuum pump. Then, flushing in open loop was started, with a flux of around 2 l/min. The whole procedure took around 24 hours. In **Figure 4-8** and **Figure 4-9** one can compare the baking cycle performed by the company and the one performed in house on the samples.
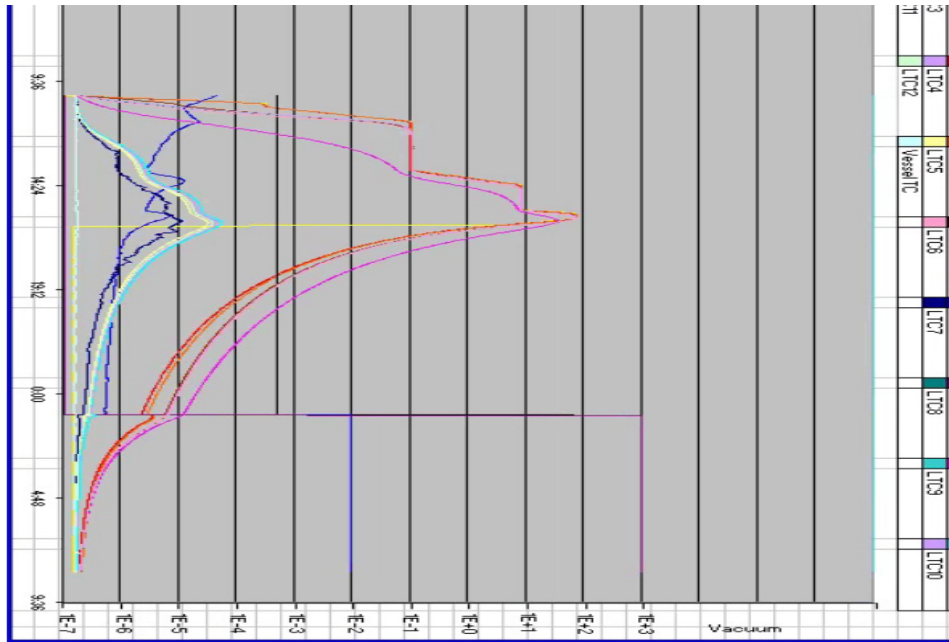
Figure 4-8: Baking cycle performed by the company on the brazed copper-stainless steel samples. Temperature and pressure curves are shown superimposed. The reference curve for setting up the in-house baking cycle are "TC controllo" (red) and "TC sicurezza" (orange)
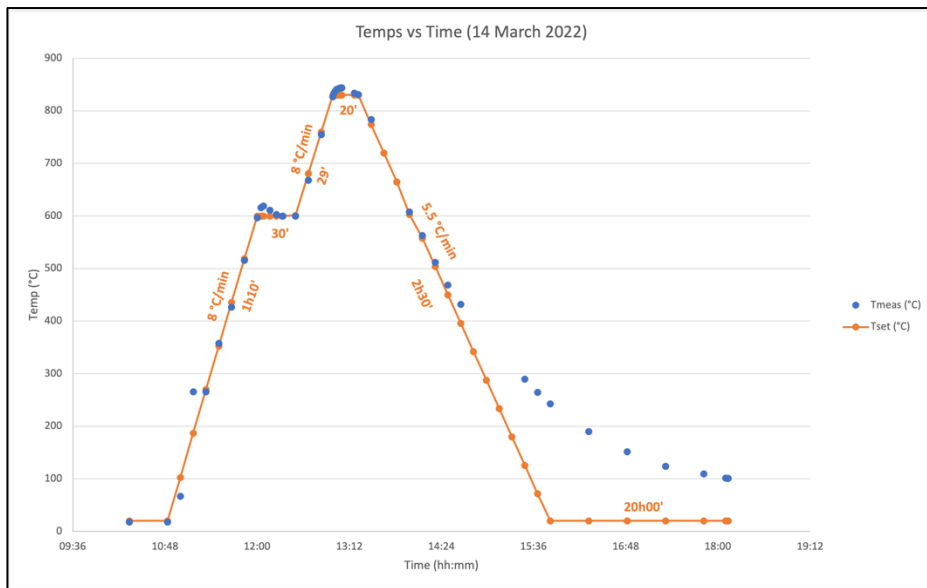

Figure 4-9: Baking cycle performed with UniMi oven on samples 3 and 4. Set and measured temperatures are reported for the whole cycle.

4.10   Cryogenic Sample 3

4.10.1   Yield Strength test

This test was successful. Cooling cycle details.

- Cool-down time: **345 minutes**.
- Cooling rate: **0.62 K/min**.
- Target temperature: **77 K**.
- Operating pressure: **0.6 bar(a)**.
- Pre-load on sample: **100 N**.
- Cross-beam speed: **0.2 mm/min**.

The result of the test is reported in Figure 4-10.
$E = \sigma / \varepsilon = 97.2$ GPa;
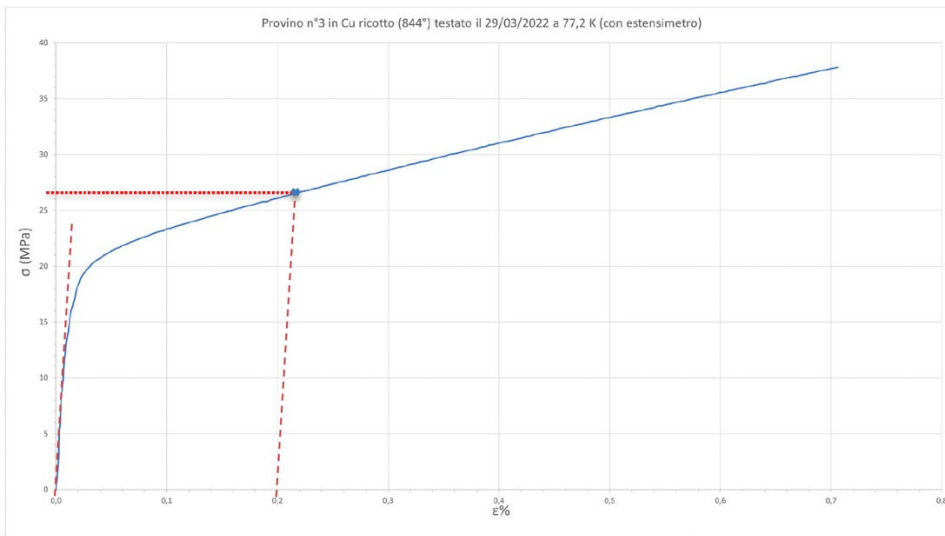Rp0.2 = 26.6 MPa.

Figure 4-10: stress vs strain plot for sample 3. Dashed lines ease identification of Rp0.2 value

4.10.2 Ultimate Stress test

Cooling cycle details.
- Cool-down time: **300 minutes**.
- Cooling rate: **0.71 K/min**.
- Target temperature: **77 K**.
- Operating pressure: **0.6 bar(a)**.
- Pre-load on sample: **100 N**.

The result of the test is reported in **Figure 4-11**. The sample broke down slightly outside the gage length. Visual inspection shows that the sample is much more elongated (the material is much softer) and the deformation in this case is also evident on the sample heads (see **Figure 4-12**).
Ultimate stress **Rs = 320 MPa** ;
Elongation **ΔL = 24.26 mm** (L0 = 46.3 mm);
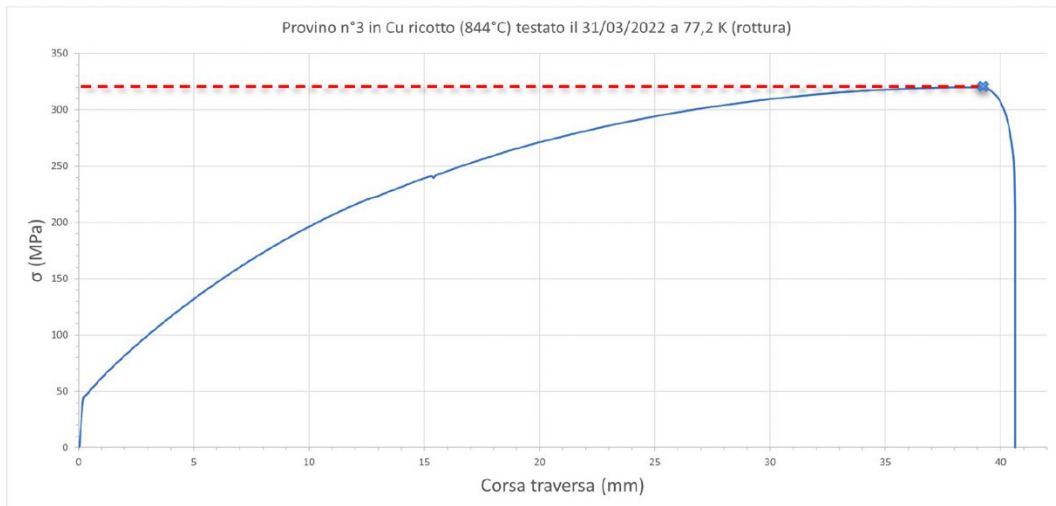% elongation **A% = 52.8%**.

Figure 4-11: stress vs crossbeam displacement for sample 3. The dashed line eases identification of the Ultimate Stress value

Figure 4-12: Comparison among three samples: untested (right); tested without baking (center); tested after baking (left). It is evident how the baking affects the sample mechanical properties, with the material becoming much softer and loosing elasticity. Plastic deformation sets in much earlier (Rp0.2 ten times smaller), whereas the value of breakdown is around 82% that of the hardened material.

4.11 Cryogenic Sample 4

4.11.1 Yield Strength test

Samples 3 and 4 were measured again after baking. For sample 4 it was found **S1=S2=S3 = 3 mm** (instead of 2.9 mm). The **Resisting Section** is therefore modified from 34.8 to **36 mm2**. This test was successful. Cooling cycle details.

- Cool-down time: **330 minutes**.
- Cooling rate: **0.64 K/min**.
- Target temperature: **77 K**.
- Operating pressure: **0.6 bar(a)**.
- Pre-load on sample: **100 N**.
- Cross-beam speed: **0.2 mm/min**.

The result of the test is reported in Figure 4-13.
E = σ / ε = 95.1 GPa;
Rp0.2 = 25.2 MPa.

Provino n°4 in Cu ricotto (844°C) testato il 12/05/2022 a 77,2 K (con estensimetro - prima rampa)
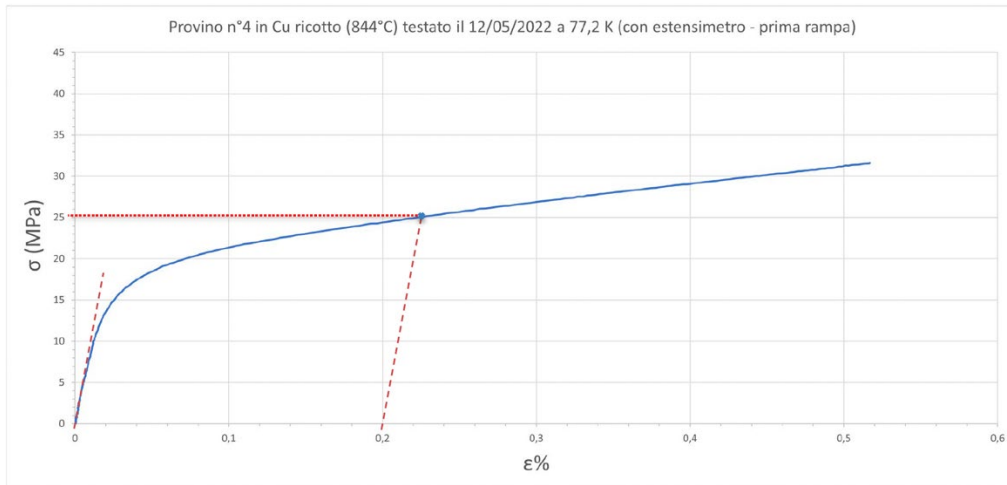
Figure 4-13: stress vs strain plot for sample 4. Dashed lines ease identification of Rp0.2 value

4.11.2 Ultimate Stress test

Cooling cycle details.

- Cool-down time: **420 minutes**.
- Cooling rate: **0.5 K/min**.
- Target temperature: **77 K**.
- Operating pressure: **0.6 bar(a)**.
- Pre-load on sample: **100 N**.

The result of the test is reported in **Figure 4-14**. The sample once again broke down slightly outside the gage length.
Ultimate stress **Rs = 324 MPa** ;
Elongation **ΔL = 24.2 mm** (L0 = 46.8 mm);
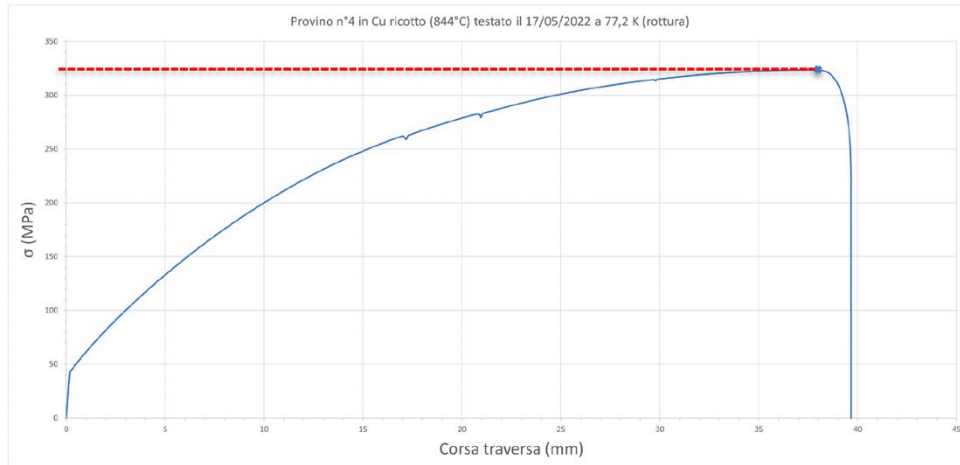% elongation **A% = 51.7%**.

Provino n°4 in Cu ricotto (844°C) testato il 17/05/2022 a 77,2 K (rottura)

Figure 4-14: stress vs crossbeam displacement plot for sample 4. The dashed line eases identification of Ultimate stress value

4.12 Hardening of baked samples during tests

The results reported above for samples 3 and 4 refer to the first deformation test. However, for both samples up to three cycles were performed with strain gauges, in order to identify possible variations in the behaviour. With very soft materials, it is expected that the very operation of tensile stress test induces some hardening of the material, and this was observed for both samples. The difference between the first and the second cycle is significant for both samples, whereas it becomes much smaller with the third cycle. As an example, **Figure 4-15** shows the first two curves recorded for sample 4.

Provino n°4 in Cu ricotto (844°C) testato il 12/05/2022 a 77,2 K
(con estensimetro - confronto tra prima e seconda rampa)
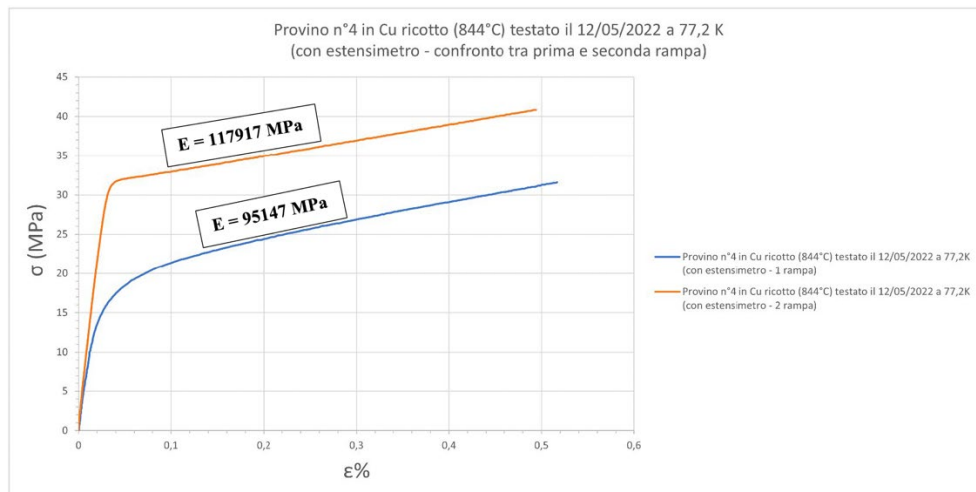
E = 117917 MPa

E = 95147 MPa

Figure 4-15: stress vs strain curves for sample 4. Here the comparison between first (blue) and second (orange) cycle shows the hardening of the soft baked samples.

The Young modulus changes from 95.1 GPa to 117.9 GPA; the Rp0.2 from 25.2 MPa to 35.7 MPa.
A similar variation is witnessed for sample 3, where Rp0.2 changes from 26.6 MPa to 42 MPa.

4.13 Derivation of effective curves

For the sake of the simulation, it was deemed necessary to obtain a "stress-vs-strain" curve with a range reaching the ultimate stress value. This would work as input for the simulation. Unfortunately, it is not possible to obtain this curve with the rupture test, as in that case the strain gauge is missing and only the crossbeam displacement is available. However, after internal discussions it was decided to try and produce an "effective curve" to be used in the simulation, starting from a number of reasonable assumptions. The starting point is to identify a way to convert the crossbeam displacement into a % strain. This was done successfully for sample 3, for which the rupture test showed a value of yield stress very close to the one of the second (last) yield strength test with strain gauge. This value, 42 MPa, follows from the initial hardening of the sample achieved during the first cycle.

The procedure can be summarised as follows:

- First, one should realise that in baked samples also the heads deform significantly (see **Figure 4-12**. Therefore, in order to remove that effect, one has to rescale the crossbeam displacement to the actual variation of the gage length during the test.
- The rescaled displacement data are then converted into a % deformation with respect to the original gage length.
- As a cross-check, one should re-obtain the % deformation experimentally measured on the sample at rupture.

As a result, one obtains a stress-strain curve that covers the range up to rupture. For consistency, the first part of this curve is compared with the one from the yield strength test. For sample 3, the match between the two curves was almost perfect, which made it possible to produce a single "effective curve". This would contain precise strain data up to around 0.35%, and then the less precise data afterwards. Despite the significant uncertainty that should be attributed to the datapoints of such curve, we estimated it a reasonable input for the simulation. The curve is shown below in **Figure 4-16**.
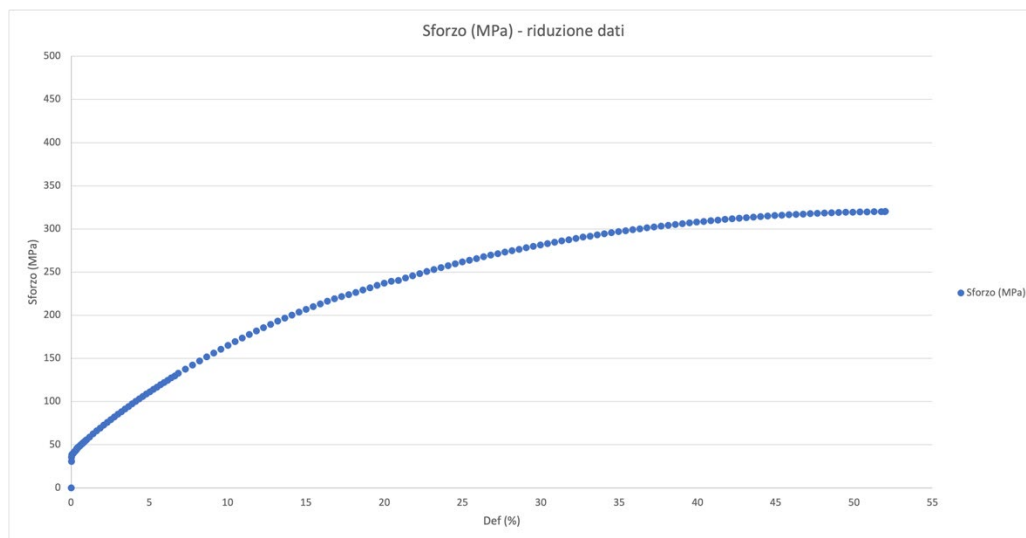

Figure 4-16: Effective curve for sample 3, obtained combining data from yield strength test and rupture test. Details in text.

Finally, it should be noted at this point that all the curves and data shown here are performed under the implicit assumption of using the so-called "engineering stress and strain", introduced in **Section 4.3.1**. In this range, the engineering and true stress/strain can be assumed identical. However, it is important to try and derive the true effective curve that one obtains when considering the deformation of the sample cross-section during the rupture test.

Below, we show what we obtain for the effective curve derived above, when correcting the data for relations **(4.2)** in **Section 4.3.1**.
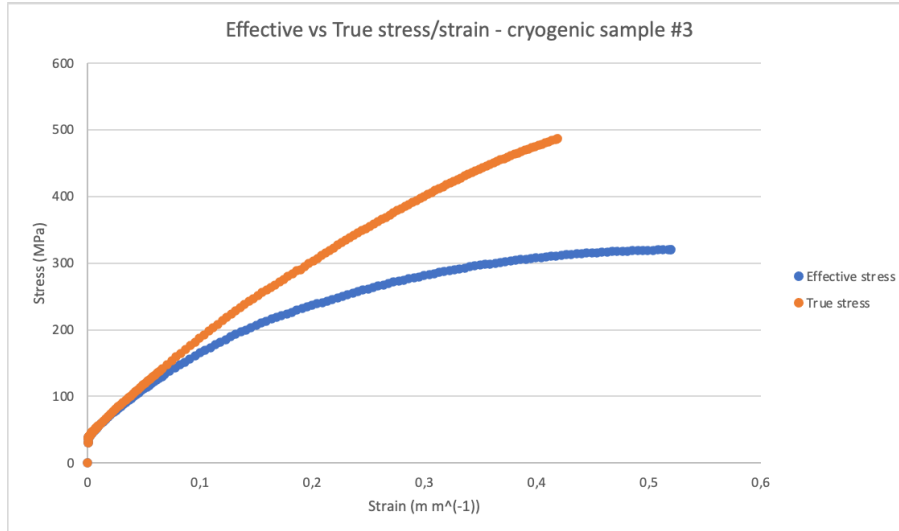

Figure 4-17: true stress vs true strain plot of sample 3, compared with the respective effective curve (see Figure 4-16) from which it was derived.

The figure shows that the true stress increases in a non-negligible way: this is due to the significant change in the sample cross section during the test. This is indeed the case for all samples and in particular the baked ones, see **Figure 4-12**. It should be reminded that this is in any case an approximation, as a continuous measurement of the deformation of the sample in the rupture area would be needed, to extract the precise values of true stress/strain.

4.14   Room temperature tests

The data extracted from the cryogenic tests are fundamental, as the literature data is scarce on copper, as already mentioned. Therefore, they are the primary input for the FEA simulations described in the next chapter. However, in order to better constrain said simulation, experimental data on the same samples at room temperature would be very required as well. For this reason, we decided to perform a new set of measurements at room temperature.

Unfortunately, the company that produced the chamber was only able to provide spare material (copper), and not to produce a new set of samples. Therefore, the Servizio di Progettazione Meccanica of INFN Milano volunteered to prepare new samples, starting from the spare copper available.

In order to obtain four samples from the available copper sheets, and to abide to the regulation UNI EN 10002 in terms of sample shape, the dimensions of the new set of samples were slightly modified, with respect to the original ones. This, however, does not imply a difference in the behaviour of the material during the tests, as the norm is respected. Technical drawing, with dimensions, of the new samples is reported in **Figure 4-18, Left**; whereas the actual samples are pictured in **Figure 4-18, Right**.
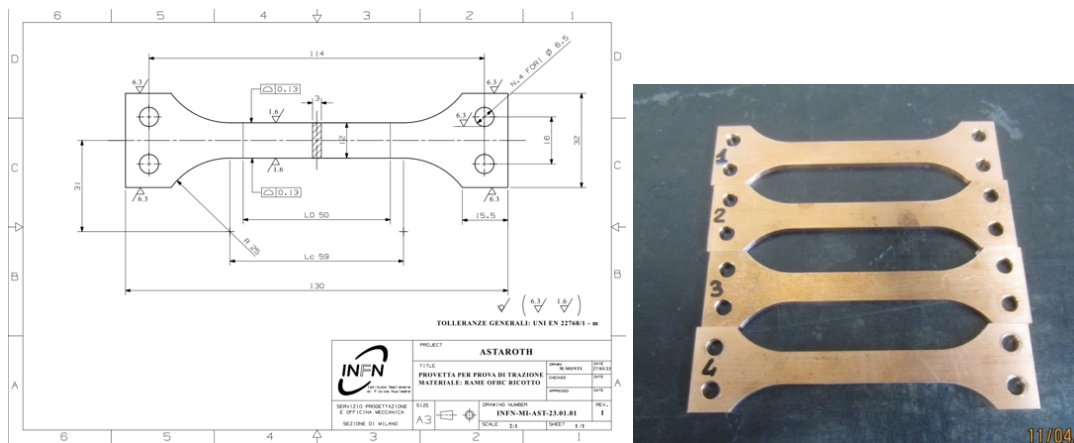
Figure 4-18: Left: Technical drawing and dimensions for the samples produced at INFN Milano for the room temperature tensile tests. Right: picture of the produced samples.

Samples were baked with the same oven and heating cycle used for the samples involved in the cryogenic tests. The baking was performed on all samples, as this is the condition of the material in the actual chamber. Please refer to **Section 4.9** for details about the baking.

The tests at room temperature were performed at LASA as well, and they exploited the very same INSTRON Machine used for the cryogenic tests. The difference in this case is that the tests were carried out simply by connecting the central shaft to the crossbeam, without installing the cryostat (see **Figure 4-2** for reference). Therefore, during these tests, the samples were visible all the time to the users.

4.14.1   Test results: introductory remarks

Room temperature tests are more standard than cryogenic tests, and no particular preparation is required, with respect to what was described in previous section. Test are carried out, as mentioned, with the sample exposed to air and visible to the tester. Since no time is allocated for cool-down and warm-up, and sample preparation requires minutes, all four samples were tested during the same day. The results of such tests are presented in the two subsections below.

As mentioned, all samples were measured for dimensional check before testing, in different positions across their length, as done for the cryogenic samples. Summary of the measurements is reported in **Table 4-4**, with reference to **Figure 4-19**.

Each sample underwent four cycles with strain gauges, to evaluate Yield Strength; later, it underwent an Ultimate Stress test, without strain gauges and leading to rupture. Following data analysis, all samples show continuous hardening with each cycle, and indeed this was found to be still ongoing during the rupture test.

For all tests and samples, the following pre-conditions are set:

- Pre-load on sample: **100 N**.
- Initial crossbeam speed: **0.2 mm/min**.

	Pos 1	Pos 1-s	Pos 2	Pos 2-s	Pos 3	Pos 3-s	Pos 4	Pos 5	Length
S. #1	11.986	3.00	11.985	3.00	11.987	3.00	11.980	11.980	129.98
S. #2	11.991	3.00	11.991	3.00	11.992	3.00	11.980	11.980	130.00
S. #3	11.992	3.01	11.993	3.01	11.991	3.01	11.990	11.990	129.94
S. #4	11.995	3.02	11.994	3.03	11.995	3.02	11.990	11.990	129.97

Table 4-4: summary of sample dimensional checks. "Pos x" columns refer to sample width; "Pos x-s" columns to sample thickness; "Length" to total sample length. All measurements are in mm. Position are referenced in Figure 4-19 .
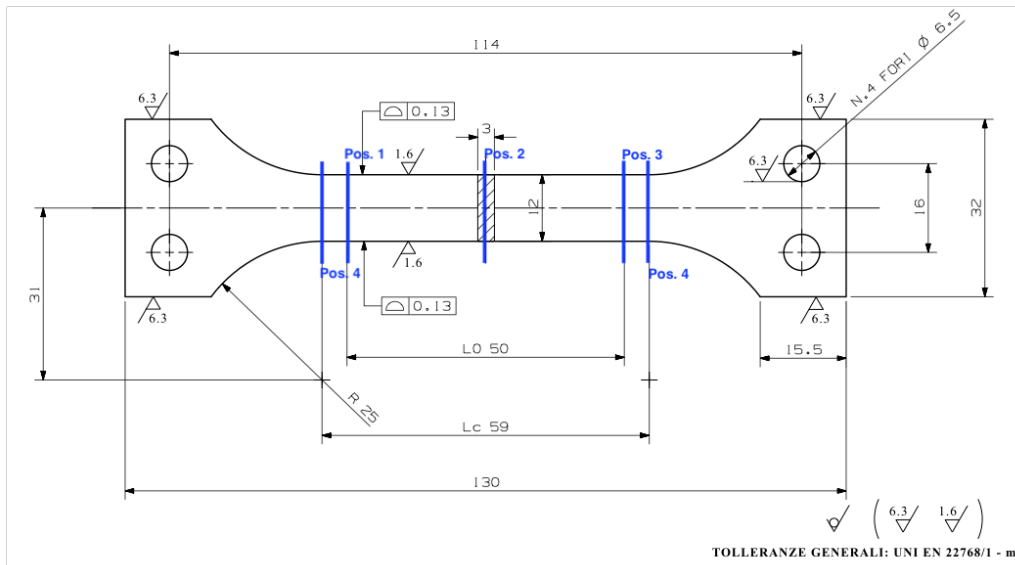

Figure 4-19: zoom on sample technical drawing with highlighted positions for dimensional checks (cfr. Table 4-4).

4.14.2   Yield strength tests

Each sample underwent four cycles with strain gauges. For all samples, Rp0.2 appears to increase linearly with each cycle, roughly by 3 MPa/cycle. The final evaluation of Rp0.2 and Young Modulus is reported here for the 4th cycle data, in **Table 4-5**.

The uncertainty on the evaluation of E, depending mostly on the range of the fit of the linear section of the curve, ranges from 2% to 10%, depending on the cycle and sample considered. It should be noted that, for all samples, the analysis was carried out on cycles 2 to 4, as in the first cycle the material is very soft, resulting in the absence of an evident linear elastic portion of the stress-strain curve. As an example, **Figure 4-20** and **Figure 4-21** below show stress-strain plot and cycle comparison for Sample #1, which has intermediate Rp0.2 values with respect to other samples.

	Sample #1	Sample #2	Sample #3	Sample #4
E = σ / ε (GPa)	55.9	53.9	54.8	54.4
Rp0.2 (MPa)	19.2	17.5	20.4	20.0

Table 4-5: Summary of mechanical characteristics obtained from Yield strength tests at room temperature.
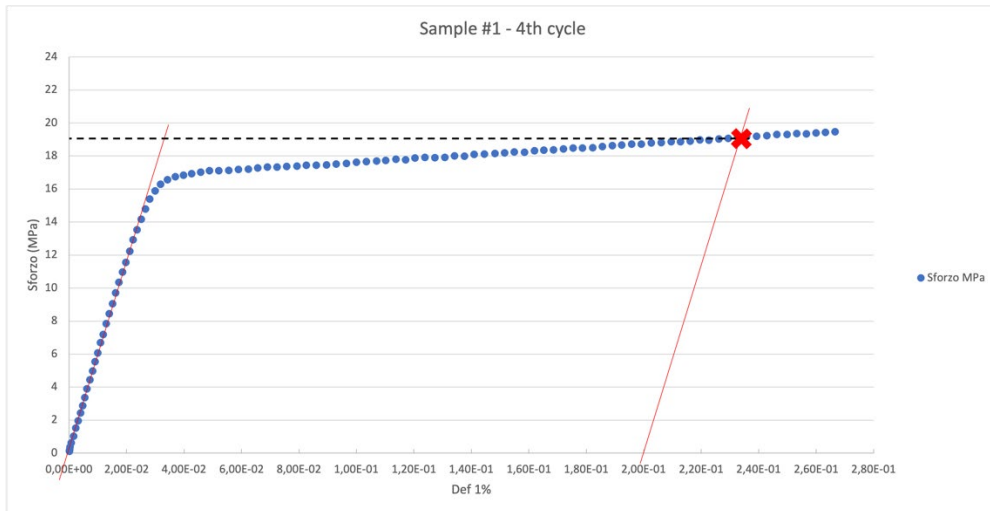
Figure 4-20: stress vs strain plot for sample 1, Room Temperature. Dashed lines ease identification of Rp0.2 value.
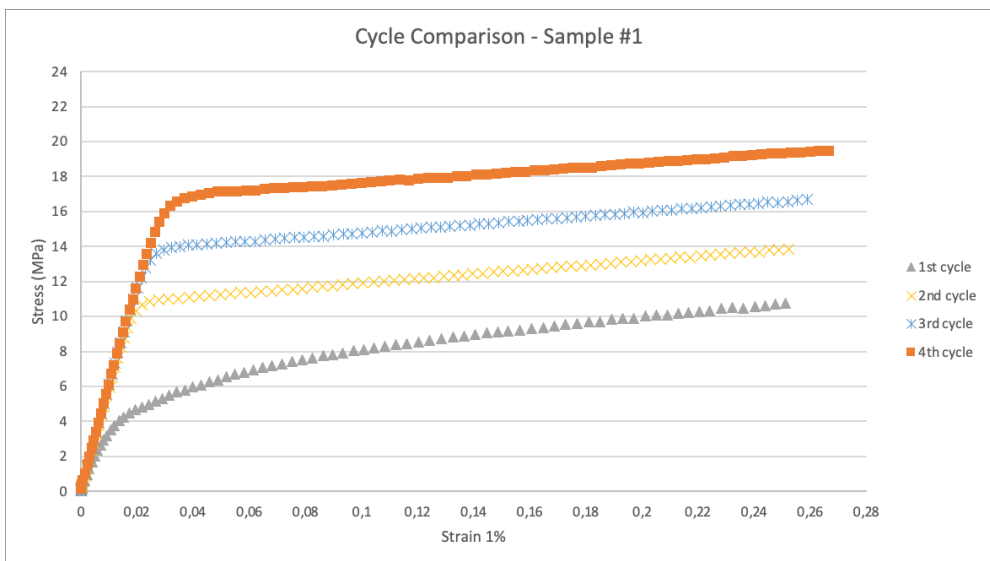

Figure 4-21: superposition of four cycles for sample 1, Room Temperature. It is evident that the sample starts out very soft (almost missing linear portion of the curve in cycle 1) and keeps hardening with each cycle.

4.14.3   Ultimate stress tests

Each sample was tested up to rupture, without strain gauges. The first three samples show standard curves, whereas the fourth one showed some issues, with the stress not increasing for the first 0.1 mm of run of the crossbeam. This poses some doubts on the validity of the specific test; however, the results are reported anyways (with an asterisk).

For each sample, Ultimate stress (**Rs**), elongation (**ΔL**) and % elongation (**A%**) are reported in **Table 4-6** below. As a reference, it is reminded that the gage length for all samples is **L0** = 50 mm.

	Sample #1	Sample #2	Sample #3	Sample #4
Rs (MPa)	198.5	196.7	199.4	197.6*
ΔL (mm)	27.3	28.7	27.8	27.3
A%	54.6	57.4	55.6	54.6

Table 4-6: Summary of results from the ultimate stress tests of the four room temperature samples. Rs for sample #4 is marked with an asterisk for issues with data collection (see text for details).

Below, **Figure 4-22** shows stress evolution again for sample #1. It should be reminded that in this specific test, lacking the information from the strain gauge, stress is plotted against the run of the INSTRON machine crossbeam. Finally, **Figure 4-23** shows the samples after rupture: it can be noted that in this case all samples broke within the gage length limits. As well, one can note that the samples heads suffered minimal deformation, differently from the samples tested at cryogenic temperature.
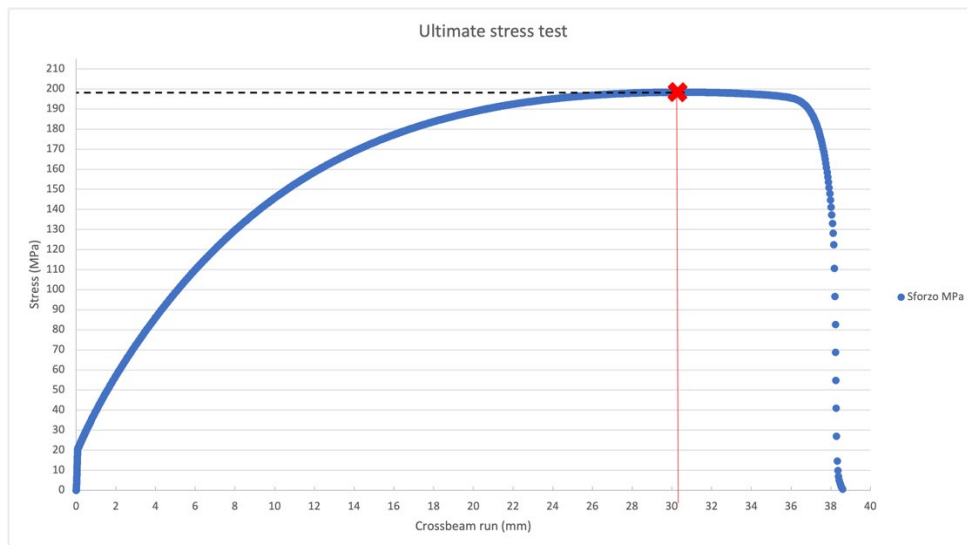

Figure 4-22: stress vs crossbeam displacement plot for sample 1, Room Temperature. The dashed line eases identification of Ultimate stress value.

Figure 4-23: Room temperature samples after rupture test.

4.15 Room temperature tests: effective and true stress/strain

It should be reminded here that tests with strain gauges are performed up to few times the value of Rp0.2; whereas rupture tests lead to the break in the samples. However, the resulting curves of the two sets of tests cannot be tied directly, as the second one shows stress evolving as a function of the displacement of the cross-beam. In order to produce a complete, effective stress-strain curve, a procedure was performed that is similar to what was done for the samples of the cryogenic tests (see **Section 4.13**). However, two main differences with respect to the previous set should be taken into account:

- as mentioned, the deformation of the heads of the samples was far less significant than in the case of the cryogenic test (see: **Figure 4-23**);
- the samples were still hardening at the rupture test. For this reason, after converting the crossbeam movement into strain measurement, the stress-strain curve of the rupture test resulted parallel but displaced, with respect to the curve of the last (fourth) cycle performed with the strain gauge. Therefore, it was necessary to rescale the ultimate stress curve to match it with the curve of the last (fourth) cycle performed with the strain gauge, in order to obtain an effective curve. The final curve is shown for Sample #1 in **Figure 4-24** (blue dots).

Afterwards, once again it is necessary to translate this effective stress-strain curve into a true stress-true strain curve, which takes into account the strong deformation of the sample in the final part of the ultimate stress cycle, leading to rupture. As described in **Section 4.13**, this is done by exploiting relations **(4.2)**. The resulting curve is shown in **Figure 4-24** (orange dots), and it represents the actual input submitted to the simulation program.
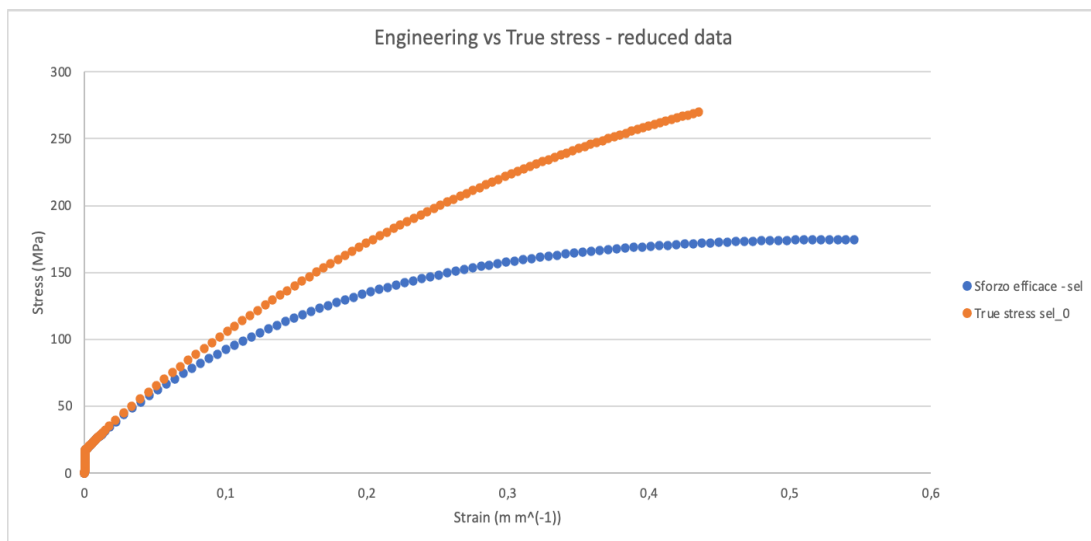

Figure 4-24: effective stress-strain curve, and true stress-strain curve, obtained from sample #1 test at room temperature. Details on the derivation of the curve in text.

4.16 Final considerations on the tensile tests.

The characterization campaign of the copper for the ASTAROTH cryogenic chamber resulted in a very interesting activity. The scarcity of literature data for copper at cryogenics temperature led to the need to perform the full material characterization in house. This work was only made possible thanks to the support of the INFN MI Officina Meccanica and of the personnel that operated the INSTRON machine. It should be evident by now, however, that the characterization could not be performed with an overall standardized procedure. The number of samples was limited; the possibility of baking was made available only halfway through the cryogenic tests campaign, thus further limiting the statistics at low temperature.

Finally, the samples were slightly different in the two campaigns, with some defects. On the other end, during data analysis some assumptions were essentials, in order to be able to put together the data from strain-gauges tests and rupture cycles. These assumptions are discussed in text, and they are made after careful evaluation of the analysis team. However, they forcefully introduce a degree of uncertainty in the propagation of the data through to the effective true stress-true strain curves. Such uncertainty is difficult to evaluate in mathematical terms, and for this reason in most of the data reported here we avoid discussing the error on the obtained data. However, it should be noted that even if we had decided to avoid the testing campaign, and tried instead to summarize the scarce available literature data, we would have ended with results affected by a 50% uncertainty. Such is the spread of values for variables such as Rp0.2, Rs.

In the end, the data we collected are from the very same material used for the cryogenic chamber, and this makes it incredibly valuable for the simulation that is going to be presented in **Section 6**.

5 Bending tests on samples of brazed connection

As part of the material characterization campaign, it was necessary to test the brazed connection as well. The brazed connection cannot be simulated precisely, mainly because the brazing paste technical specifications (LSNi-2, **[11]**) do not report tensile properties at room temperature, nor there are literature data on cryogenic operations of said paste.
For this reason, the collaboration decided to perform a small-scale testing campaign as described below, exploiting samples that were prepared by the manufacturing company with the same materials and procedure (brazing under vacuum) employed for the final chamber

5.1 Test concept and setup

A set of four samples of brazed connection was requested to the manufacturing company, according to the drawing in **Figure 5-1**. The samples do not reproduce the brazing of the chamber exactly, because they lack its curvature. However, after discussing with the company, they were deemed reliable enough for the testing campaign.
The concept of this testing campaign was to try and reproduce, on the samples, the stress induced on the chamber brazed connection by the operating conditions, and then to verify the integrity of the brazing itself.
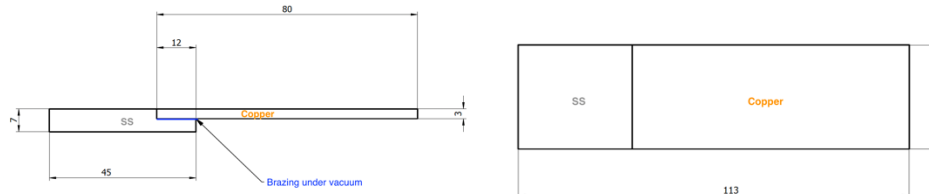

Figure 5-1: Brazed sample drawing. The area where the brazing paste is placed is highlighted in blue in the left panel

The definition of the test conditions was performed as follows:
- the whole chamber design underwent a thermo-mechanical simulation, which resulted in a stress map as shown in **Figure 5-2**. In particular, a maximum value of Von Mises stress of 57.1 MPa was obtained on the internal wall of the copper chamber, next to the brazed connection. It should be noted that this exercise was performed in Dec. 2021, on a still partially conceptual design. Details on how the simulation is performed are postponed to the dedicated section, i.e., **Section 6**.
- A simulation of a brazed connection sample was also prepared. The simulated sample was pre-loaded with the thermal load (**Figure 5-3**, panel (b)).

- A normal force was set on the sample, in the point shown in panel (a) of **Figure 5-3**. The force was increased up to the point of obtaining again 57.1 MPa in the region of the brazed connection (**Figure 5-3**, panel (c)).
- The obtained force, 50 N, was determined as the one to be used in the experimental tests on the actual samples.
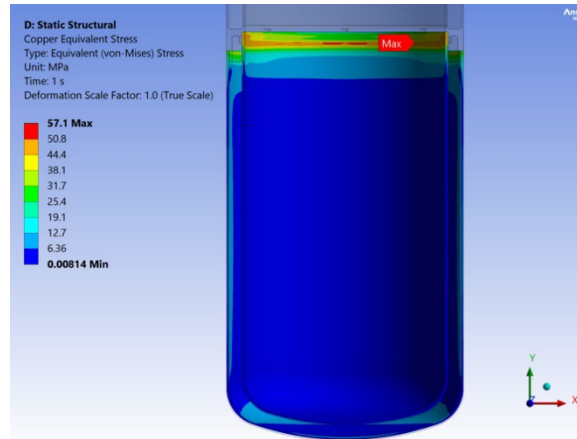

Figure 5-2: Thermo-mechanical result of the copper chamber for a still partially conceptual design. Details on the simulations will be described in the next Section.
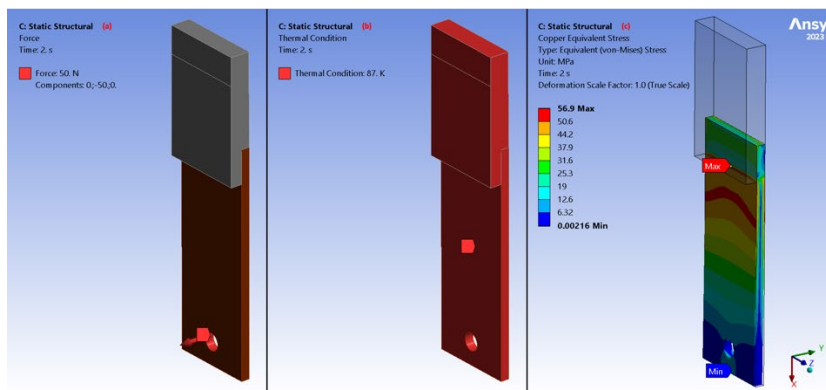
Figure 5-3: Simulation of brazed connection sample. Panel (a) shows where and how the forcer is exerted; panel (b) shows the pre-load created by bringing the sample to 87 K; panel (c) shows the Von Mises stress map obtained by using a force of 50 N.

In order to perform the tests, a dedicated support structure was built by the INFN Officina Meccanica, as shown in **Figure 5-4**. The samples were held horizontally on the stainless steel side, whereas the copper end was free. Each sample was connected, through a SS wire, to a dynamometer (*Sauter FH100*, 100 N capacity) fixed on a rail. By pulling the rail upwards, the dynamometer would measure the force exerted on the sample via the SS wire.

Each sample was dipped in LN2 before starting the bending test, in order to reproduce the chamber operating conditions. It is reminded once again that, even if the chamber will in the end operate at LAr temperature (87 K), initial testing is done with LN2, at a temperature of 77 K. The difference in temperature is not significant in the characterization of the materials.
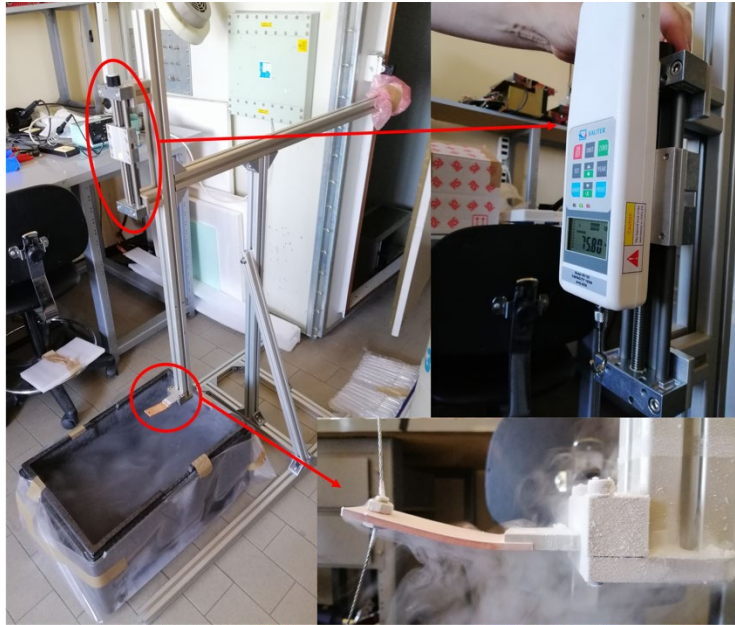
Figure 5-4: Test stand for the bending of the brazed samples, with a sample suspended above a LN2 bath. The top right insert shows the dynamometer in operating position. The bottom right insert zooms in on a bent sample: the connection point, i.e., the point where the pulling force is exerted, is clearly visible.

Each sample therefore underwent the following cycle:
- Cooling down to 77 K in LN2.
- Bending test, performed by pulling from the dynamometer on the rail.
- Release of force.
- Extraction of the sample; warm-up in atmosphere.

Of the four samples, two were bent to the defined nominal force (50 N), whereas two others were placed under a force of 75 N, thus adding a 1.5 factor.

5.2 Test results and considerations

Below, in Errore. L'origine riferimento non è stata trovata., the summary of the four tests is presented. For each sample, bending force and deformation is reported. Deformation is intended as maximal vertical deviation of the top face of the sample, with respect to the nominal horizontal, unbent, configuration.

Sample #	Force (N)	Deviation (mm)
1	75	17.3
2	75	15.9
3	50	8.3
4	50	10.5

Table 5-1: Summary of forces imposed, and resulting measured deviations, on the four brazed samples.

For a bending force of 50 N, the deformation calculated by FEA is much smaller than the experimental evidence. Then, increasing in the analysis the bending force up to 70 N, the deformation becomes comparable to the value obtained by testing the sample with a bending force of magnitude 75 N. The deformation grows fast over 65 N in the simulation: this is due to the fact that, at the time the simulations were performed, the isotropic hardening of copper was based on hypothetical simplified bilinear curves, as the results of the tensile tests of the samples, described in Section 4, were not yet available.

Samples were later examined under the microscope, aiming to detect disconnections and/or cracks on the brazed connection. No such feature was identified.

Samples finally underwent x-ray scan. The comparison of samples scans before and after the tests, once again, did not highlight any change in the brazed connection.

To the best of the collaborators capability, this was taken as demonstration of the robustness of the brazed connection under operating conditions, for the final chamber.

It should then be noted that in at least two out of four tests, a safety factor of 1.5 was included, by raising the pulling force to 75 N. Furthermore, the final simulations on the as-build model of the cryogenic chamber reported an updated maximal Von Mises stress on the copper of 37.9 (see **Section 6**). This means that the value considered for the experimental tests was higher than in reality, thus adding a further safety factor of about 1.5.

Overall, at least two samples ended up being tested with a safety factor of around 2.25, thus yielding strong confidence in the robustness of the brazed connection of the cryogenic chamber.

6 Finite Element Analysis (FEA)

The design choices of the ASTAROTH cryogenic chamber, before proceeding to construction, has been validated from the point of view of heat transfer efficiency, mechanical deformations/stresses and structural stability.

This has been achieved by developing a 3D nonlinear multiphysics model, based on coupled thermo-mechanical simulations, by means of the Finite Element Analysis (FEA), using *ANSYS*® software.

6.1 Thermal FEA

From the thermal point of view, the cryogenic chamber must allow a safe and uniform cooling down of up to two cubic NaI(Tl) crystals, respecting the thermal requirements of a uniform temperature of the crystals within 0.1 K, under a maximum temperature of 150 K. To obtain these performances, the detector chamber inner temperature is tuned and stabilized by the natural cooling power provided by the external bath of LAr at 87 K, in opposition to a heating element (electrical resistance), in order to raise the temperature in a controlled way up to 150 K and keep it stable in a dynamic thermal equilibrium.

Low pressure Helium gas (100 mbar) fills the inner volume of the cryogenic chamber, serving as heat-transfer medium to the crystals, and providing the necessary thermal inertia. In order to prevent convective heat transport, three-four SS disks and a thin copper disk, all fixed on the crystals insulating support bars, are placed inside the chamber. The copper disk is the closest to the crystals. In this way, gas stratification along the chimney is favoured. The heat transfer occurs by conduction, and heat convection/radiation are evaluated to be negligible in the analysis.

The temperature distribution of the cryogenic metallic chamber, with crystals and Helium gas volume inside, related to the external LAr bath and the power of the heating element, is the main result obtained by the thermal FEA.

6.1.1 FEM model for the Thermal Analysis

The 3D FEM model has been developed by means of *ANSYS WorkBench*, starting from the "*as built*" version of the cryogenic chamber CAD model file *21094-1-00.stp*. A simplified geometry of the external dewar has been added to the original assembly, as well blind flanges to close the chimney and its two lateral ports. The CAD model, then, has been modified, operating defeaturing of the geometries, to make it suitable for the Finite Element Analysis. The geometry in FEM environment is a half of the full model, taking advantage

of the symmetry given by the radial-axial plane passing through the vertical axis of the cryogenic chamber and the axes of the two lateral ports of the chimney.

The model includes all main components: the copper chamber, the stainless-steel chimney with lateral ports, the blind flanges and the external dewar. Bolt connections, SS disks, ports on the flanges, cables and support structure for crystals have been removed from the model, being not essential for the simulation results.

The Helium gas has been modeled as solid parts filling the empty volume of the inner chamber, as its behavior is based on heat transfer conduction only.

The FEM model is shown in **Figure 6-1**: the mesh is made by four million solid elements of quadratic order, and about eight million nodes. All thermal contacts have been defined "bonded".

The detail of the thermal bridge region is shown in **Figure 6-2**: the mesh is very fine, with an average element size of 1.5 mm, in order to have at least two elements in the thickness, to catch the thermal gradient first, and then the stress gradient in the structural analysis. The parts made in stainless steel AISI 316L are gray colored in the figure, whereas copper is red. The brazing alloy is not represented in the model: copper-stainless steel surfaces of the thermal bridge, in contact, have been defined as "bonded".

The thermal simulation was performed using a high-performances workstation (CPU: AMD 24 cores - 2.80 GHz, RAM: 512 GB) and took a total computational time of 10 minutes.
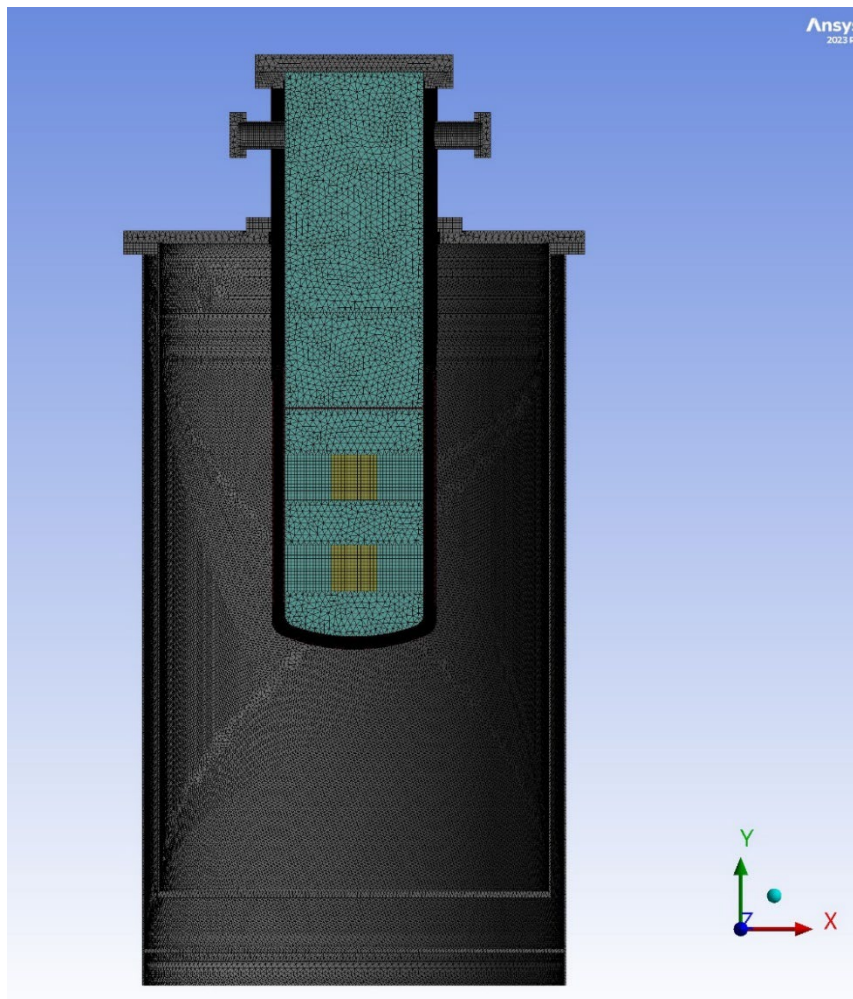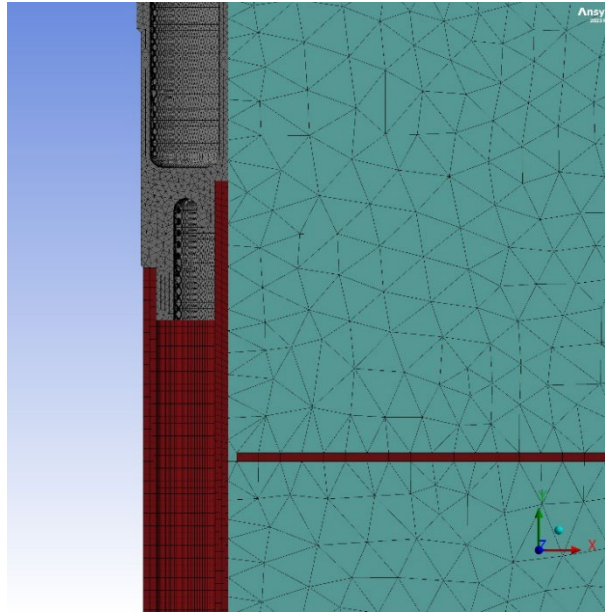

Figure 6-1: Thermal FEM model

Figure 6-2: Detail of the thermal bridge region

6.1.2 *Materials properties*

Being the Thermal Analysis purely conductive, the materials have been characterized by the coefficient of thermal conductivity, which generally varies as a function of the temperature. The data used in *ANSYS* for the simulation are shown below.

Figure 6-3 shows the *ANSYS* diagram of the isotropic thermal conductivity of the copper C10200 OFHC annealed, while **Figure 6-4** shows the *ANSYS* diagram of the isotropic thermal conductivity of stainless steel AISI 316L annealed: both are dependent on the temperature.
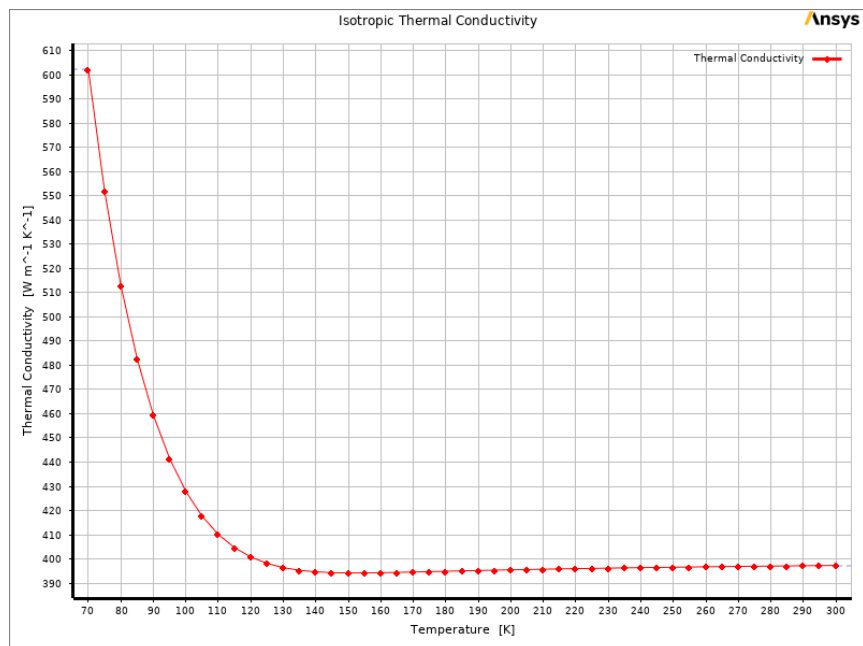
Figure 6-3: Copper C10200 OFHC annealed - thermal conductivity
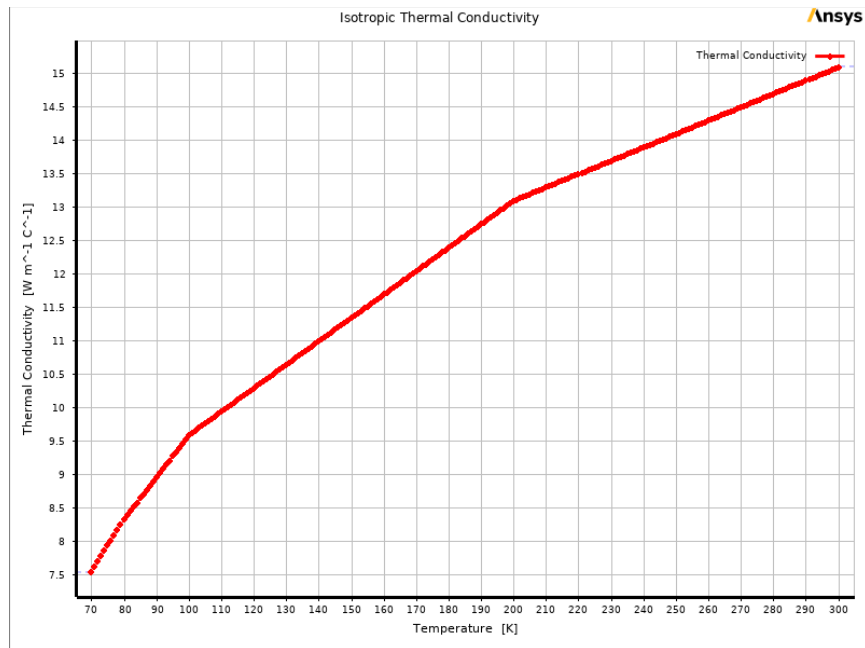
Figure 6-4: AISI 316L annealed - thermal conductivity

The coefficients of thermal conductivity of OFHC copper and AISI 316L are very different. This is a precise design choice, in order to have the bridge that brings the cooling power from the liquid bulk to the inner volume sufficiently thermally resistive, to avoid a fast cool-down of the crystals.

Figure 6-5 shows the ANSYS diagram related to the isotropic thermal conductivity of Helium gas at low pressure (100 mbar), treated as conductive solid.
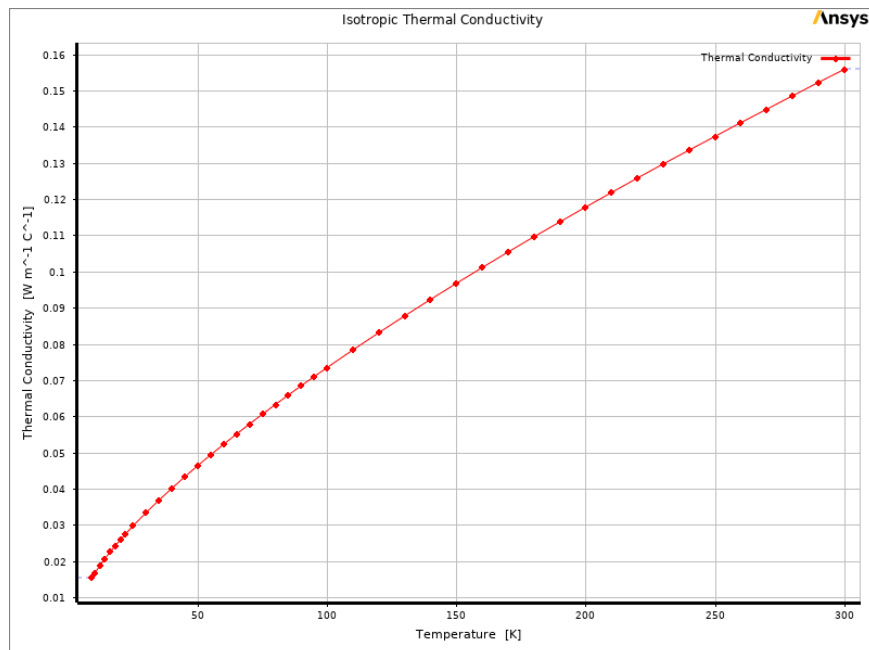
Figure 6-5: Low pressure Helium (100 mbar)- thermal conductivity

Finally, the thermal conductivity of quartz has been defined to be 10.7 W/m K, for the entire operating temperature range.

6.1.3 Settings, constraints and thermal loads of the Thermal FEA

The Thermal FEA has been performed in steady state, with an initial uniform temperature of the model set to 293.15 K. Heat transfer can only occur by conduction, no convection and no radiation thermal exchanges are implemented in the analysis, because they are considered negligible.

The constraints conditions of the analysis are, basically, fixed temperatures on some defined surfaces, as shown in **Figure 6-6**.

The main constraint condition [A], is given by the fixed temperature of 87 K, set on the wetted external surfaces (made in copper and, partially, in AISI 316L) of the cryogenic chamber, in contact with the LAr bath, and on the wetted inner surfaces of the dewar.

The temperature of the external surface of the dewar flange [B] has been fixed to 268 K, while the temperature of the external surface of the blind flange of the chimney [C] has been fixed to 288 K (both previously estimated by hand-made calculation).
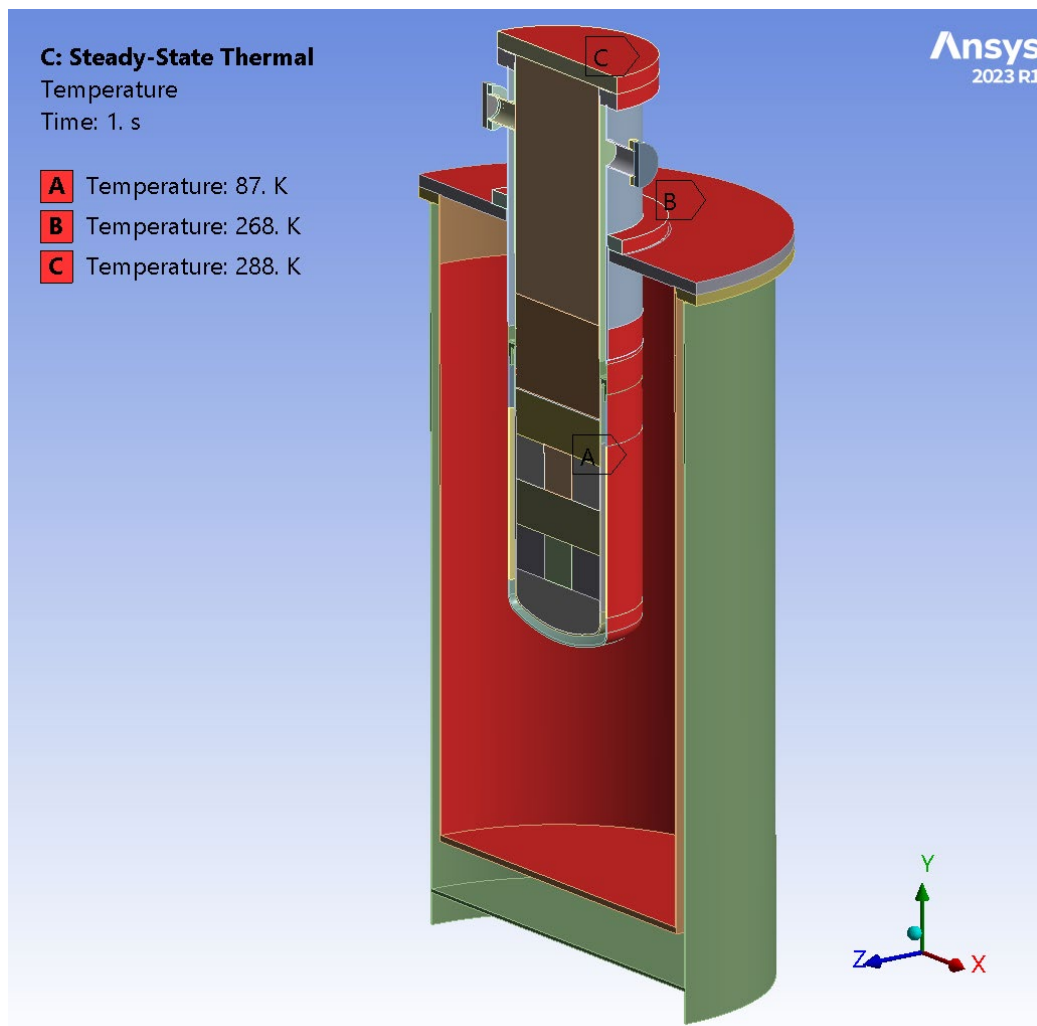
Figure 6-6: constraints of the thermal FEA

The thermal loads are shown in Figure 6-7.

The main thermal load [A] is given by the power dissipated by the heating element, an electrical resistance placed on the copper inner wall of the cryogenic chamber, about 20

millimetres above the copper separation disc. The power has been applied to a 10 mm high cylindrical surface. The power has been calculated to be 180 W for the full chamber (90 W for the half model), as resulting by several preliminary iterations of the thermal FEA: it guarantees to obtain a uniform temperature of 146 K on the crystals.

Other thermal loads are heat fluxes passing through the chimney, coming from the external environment towards the inner chamber: the heat flux [B] passing through the Helium gas column (31.3 W/m^2), and the heat flux [C] passing through the stainless-steel inner neck of the chimney (3697.2 W/m^2), both previously estimated.

The power dissipated by the sensors electronics, not applied in the analysis, is considered negligible.
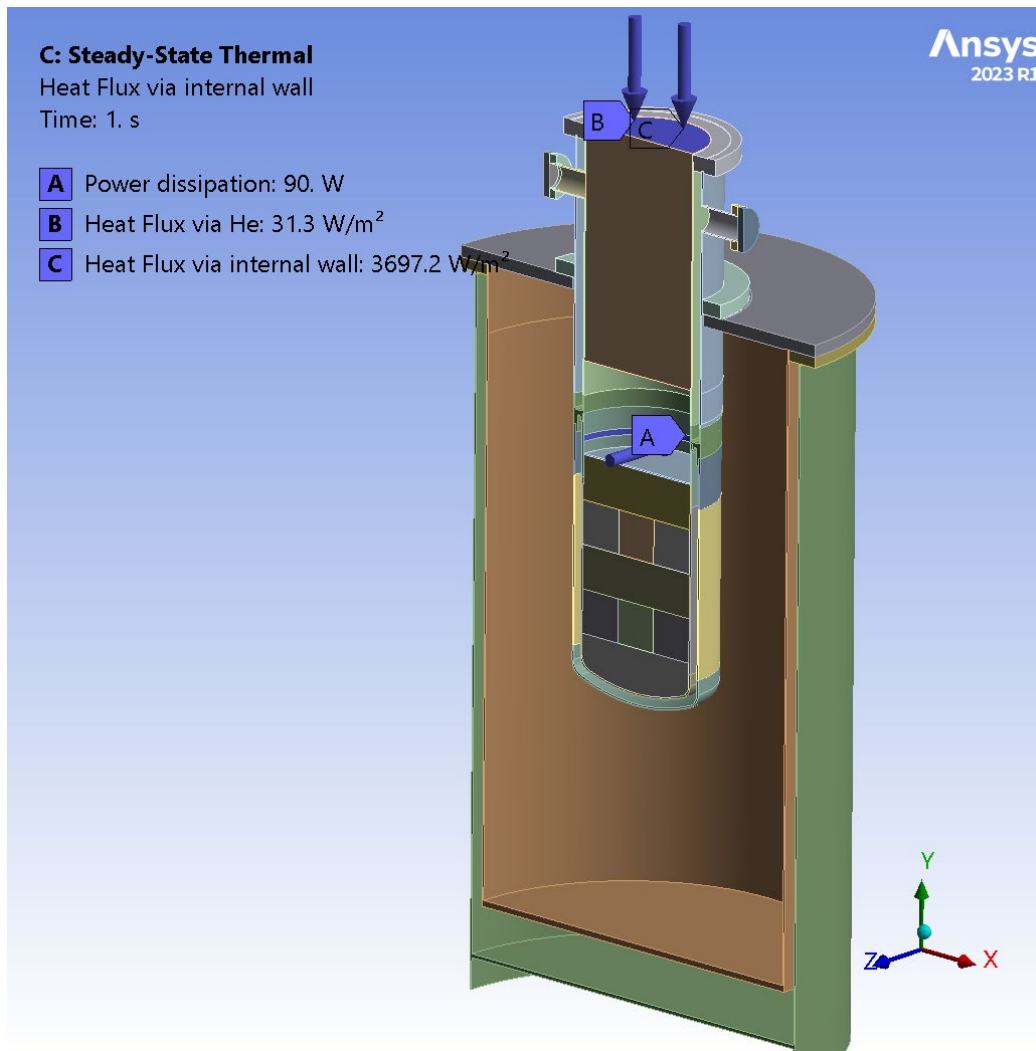
Figure 6-7: thermal loads of the thermal FEA

6.1.4 Thermal FEA results

In operating conditions, at the thermal equilibrium, the temperature contour plot of the overall ASTAROTH apparatus is shown in **Figure 6-8** on the left side, while the results for the cryogenic chamber, with the inner Helium gas, the separation disk and the crystals, is shown in **Figure 6-8** on the right side. **Figure 6-9** shows the temperature field over the copper/stainless steel bridge: it fulfills its function to create an adequate thermal gradient

between the outer wall at 87 K and the inner wall of the cryogenic chamber, obtaining a maximum ΔT of 60 K.

Figure 6-10 shows the temperature of the inner Helium volume, below the separation disk: it results to be uniform within a maximum variation of 0.05 K (145.92 K ≤ T_{He} ≤ 145.97 K), so the dissipated power of 180 W is adequate to obtain a uniform temperature, less than 150 K, inside the cryogenic chamber volume (the first thermal requirement).

The second thermal requirements is to obtain a uniform temperature of the crystals within 0.1 K, and it is fully achieved, being the maximum ΔT = 0.01 K (see **Figure 6-11**).
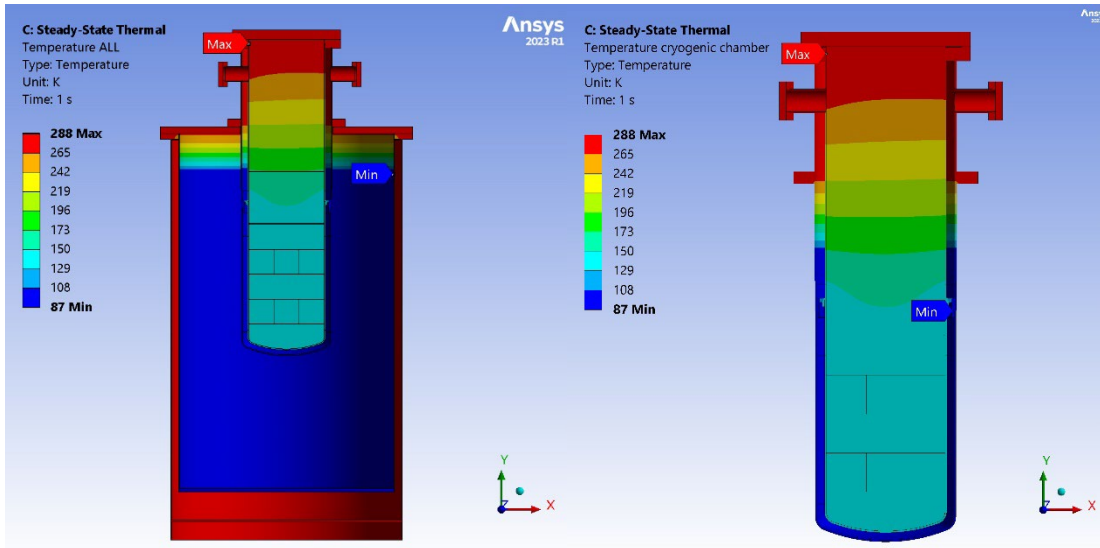
Figure 6-8: Temperature of the overall apparatus (left) and of the cryogenic chamber (right)
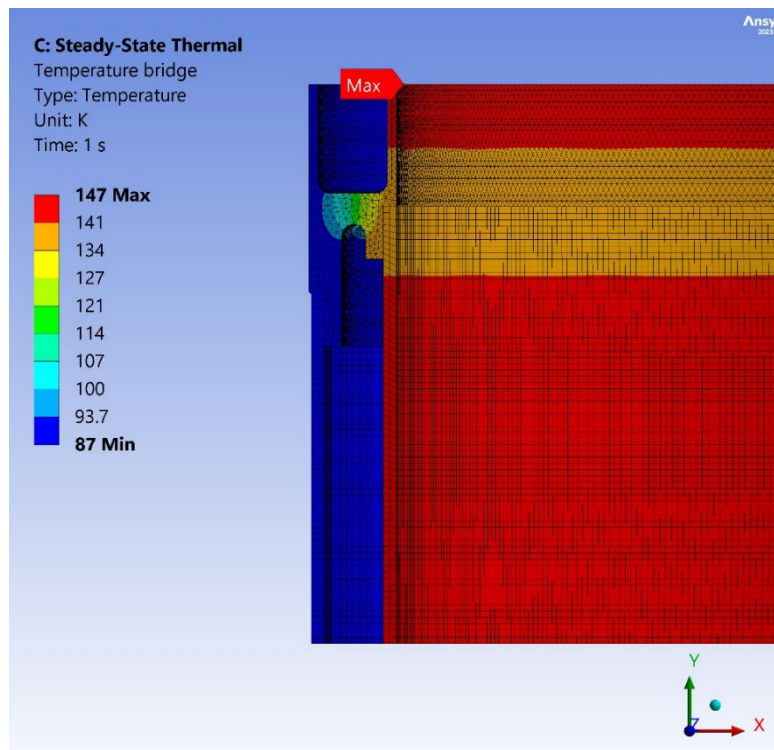
Figure 6-9: Temperature of the thermal bridge
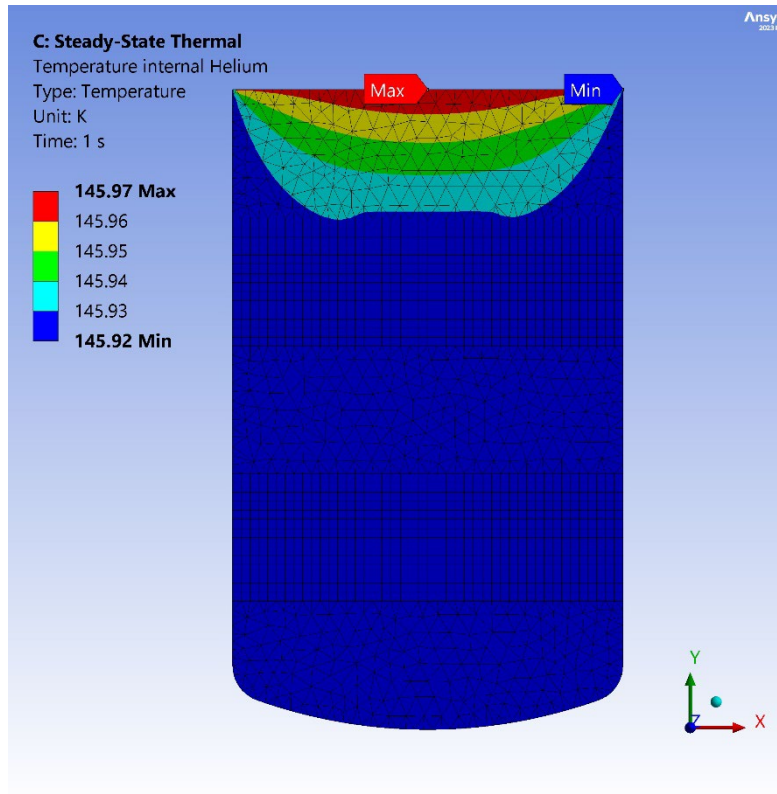
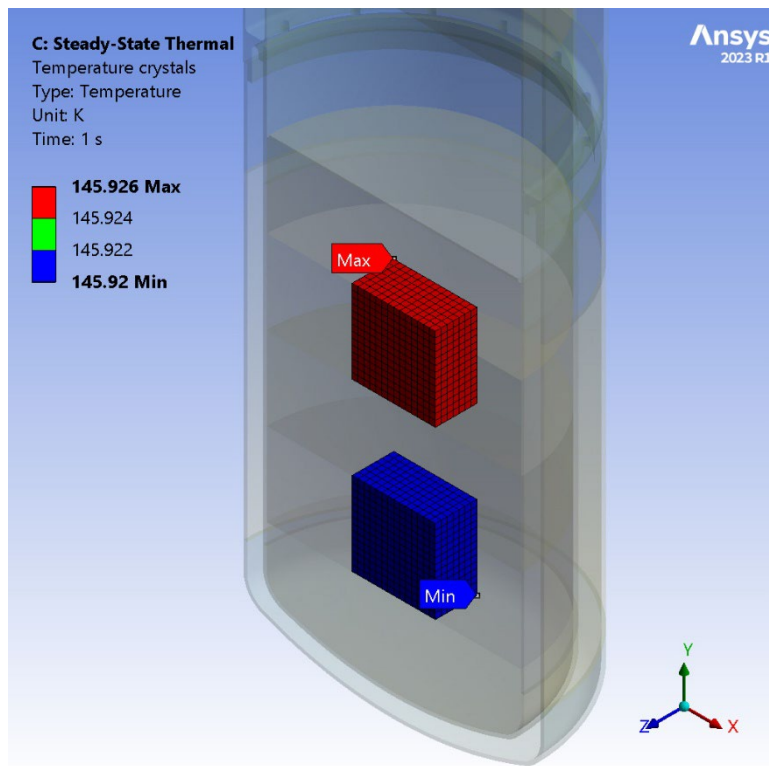**Figure 6-10: Temperature of the Helium volume**

Figure 6-11: Temperature of the crystals

6.2 Thermo-mechanical Finite Element Analysis

The Thermo-mechanical analysis has been performed to calculate mechanical stresses of the cryogenic chamber, mainly due to the CTE mismatch between copper and stainless steel, which reach peak values in the region of the thermal bridge. To perform this kind of analysis, it is necessary to import the temperature distribution on the metallic bodies, resulting by Thermal FEA, within the structural environment.

The aim of the Thermo-mechanical analysis is to verify the structural robustness of the cryogenic chamber, **in operating conditions**, basically comparing the maximum Von Mises stress calculated by FEA with the copper and the AISI 316L Yield Stress values.

6.2.1 FEM model for the Thermo-mechanical Analysis

The structural FEM model has been built starting from the thermal one, and includes almost all main components, excluding the Helium volumes, the separation disk and the crystals; these have been suppressed, being not functional for this kind of analysis.

Once again, a half model is used, symmetrical with respect to the radial-axial plane passing through the vertical axis of the cryogenic chamber and the axes of the two lateral ports of the chimney. The mesh of the thermal model has been transferred one-to-one to the structural model, switching the quadratic thermal elements to quadratic structural elements, with the same number/location of the nodes. The FEM model is shown in **Figure 6-12**: the mesh is made by 3.9 million solid elements, and about 7.5 million nodes. All mechanical contacts have been defined "bonded", including the copper chamber - stainless steel bridge connection (the brazing alloy layer is not modeled, due to its very small thickness and unknown mechanical properties). The thermo-mechanical simulation has been performed with a high-performances workstation (CPU: AMD 24 cores - 2.80 GHz, RAM: 512 GB) and took a total calculation time of 1hour.
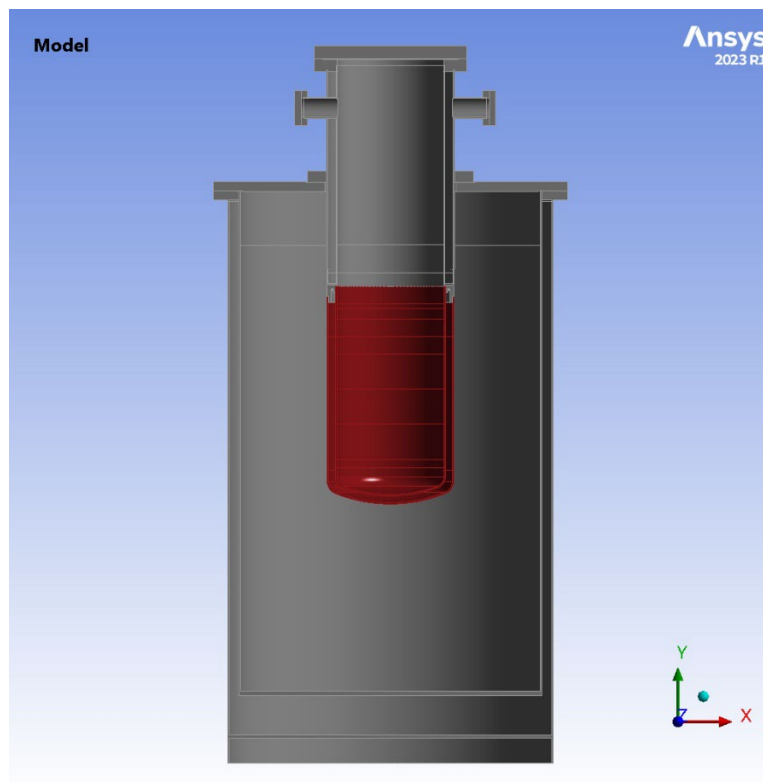

Figure 6-12: Structural FEM model

6.2.2 Materials properties

Mechanical properties of copper C10200 OFHC annealed, used to run the Thermo-mechanical FEA, are collected in **Table 6-1**. Young's Modulus, Yield Stress and UTS were measured by experimental cryogenic tensile tests at 77 K and by experimental tensile tests at the room temperature of 293.15 K, as reported in **Section 4**. Then the effective curves and the true stress/true strain curves were calculated. Data collected in **Table 6-1** refers to true strain/strain curves used in Ansys.

Physical and mechanical properties of copper C10200 OFHC annealed							
Density [kg/m³]	Young's modulus [GPa]		Poisson's ratio	Yield stress [MPa]		UTS [MPa]	
T = 293.15 K	T = 77 K	T = 293.15 K		T = 77 K	T = 293.15 K	T = 77 K	T = 293.15 K
8900	122.75	55.8	0.339	42.3	19.5	320	270

Table 6-1

Mechanical properties of stainless steel AISI 316L annealed, provided by *ANSYS* database, are collected in **Table 6-2**.

Physical and Mechanical properties of AISI 316L annealed					
Density [kg/m³]	Young's modulus [GPa]		Poisson's ratio	Yield stress [MPa]	UTS [MPa]
T = 296.15 K	T = 75 K	T = 294.26 K		T = 296.15 K	T = 296.15 K
7969	208.9	195.1	0.27	229.6	521.2

Table 6-2

In **Figure 6-13** the CTE of the copper C10200 OFHC annealed is compared to the CTE of AISI 316L annealed, as function of the temperature, in the range of interest.
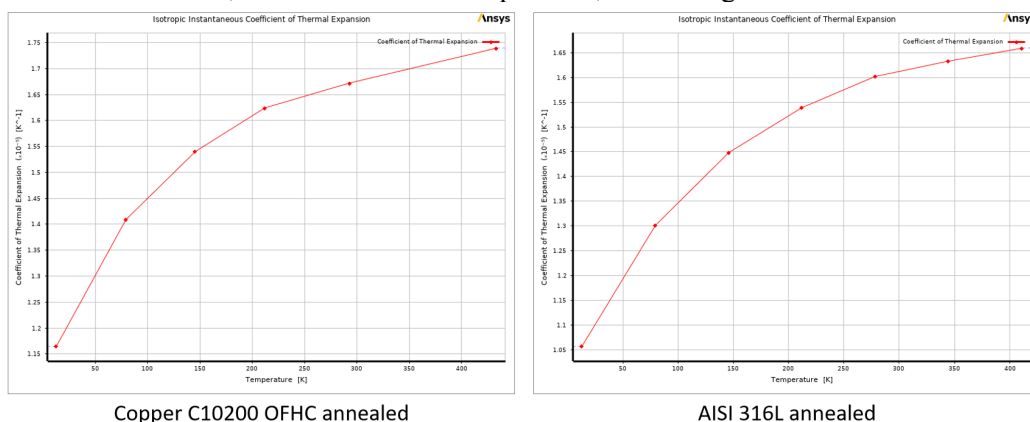

Copper C10200 OFHC annealed

AISI 316L annealed

Figure 6-13: CTE of OFHC copper compared to the CTE of AISI 316L

True stress/true strain curve of copper C10200 OFHC annealed, at the temperature of 77 K, was calculated starting from the results of the cryogenic tensile tests, as described in detail in **par. 4.13**. Then, the true stress/true strain curve has been modified in order to obtain the plastic strain curve, by removing the elastic strain (calculated via Young's Modulus) from the total strain. The **plastic strain curve has been implemented in *ANSYS* as multilinear isotropic hardening curve** (see **Figure 6-14**). The same procedure has been applied to the true stress/true strain curve of copper C10200 OFHC annealed, at the temperature of 293.15 K, calculated using the results of the tensile tests at room temperature (see **par. 4.15**), to obtain the multilinear isotropic hardening curve shown in **Figure 6-15**.
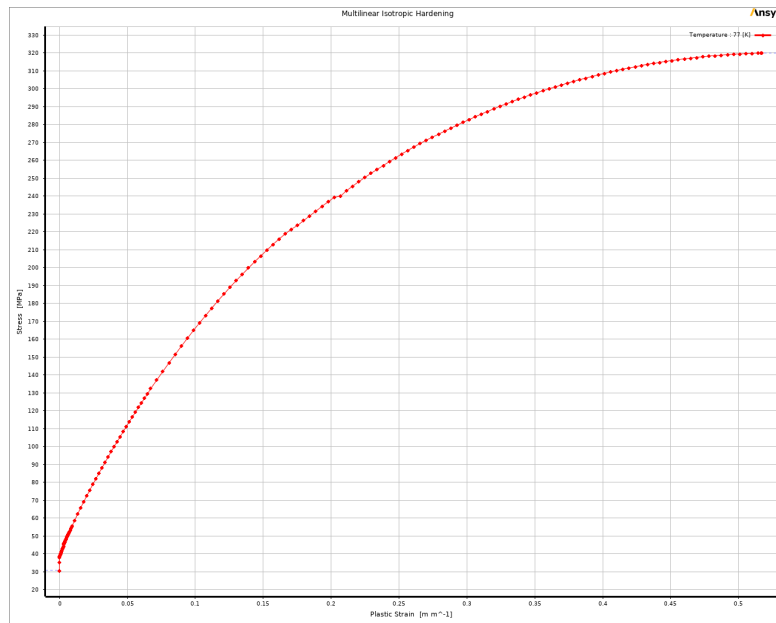
Figure 6-14: isotropic hardening curve of annealed OFHC copper @ 77 K
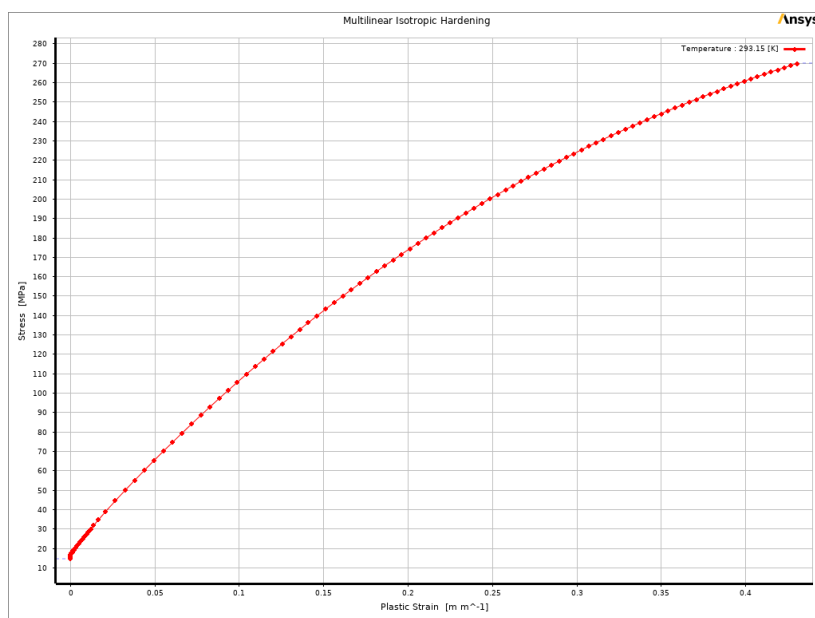
Figure 6-15: isotropic hardening curve of annealed OFHC copper @ 293 K

The multilinear isotropic stress/strain curve of annealed stainless steel AISI 316L, at the temperature of 293.05 K, by *ANSYS* database, is shown in **Figure 6-16**Figure 6-15.
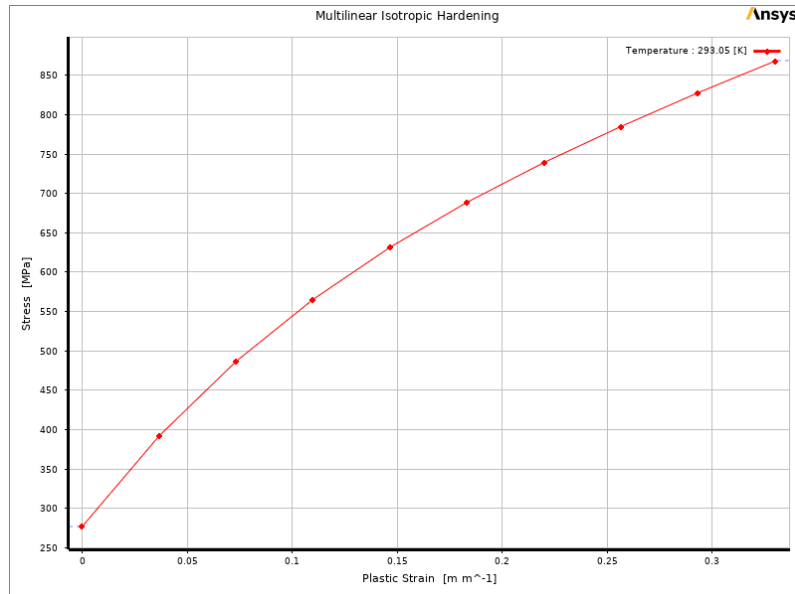

Figure 6-16: isotropic hardening curve of annealed AISI 316L @ 293 K

6.2.3 *Constraints of the Thermo-mechanical FEA*

The constraint condition of displacement equal to zero, along the vertical Y axis of the cryogenic chamber, has been imposed on the annular surface at the base of the external dewar, that is, in fact, the surface laying on the floor (constraint A, **Figure 6-17**).

To make the model isostatic, avoiding movements in X-Z plane, a little circular region, in the middle of the external dewar bottom surface, has been constrained with zero displacements along X,Z axes (constraint B, **Figure 6-17**); in this way the thermal contraction of the metallic structures, during the cooling down, can occur without unrealistic constraints.
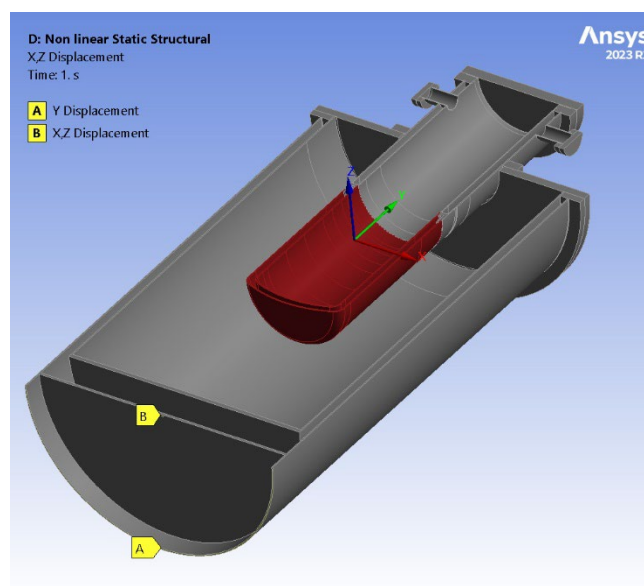

Figure 6-17: Constraints of the structural FEM model

6.2.4 *Loads of the Thermo-mechanical FEA*

The temperature field resulting on the metallic bodies, by the thermal analysis, has been imported into the structural environment, to calculate the effect of the thermal contraction during cooling down (see **Figure 6-18**).
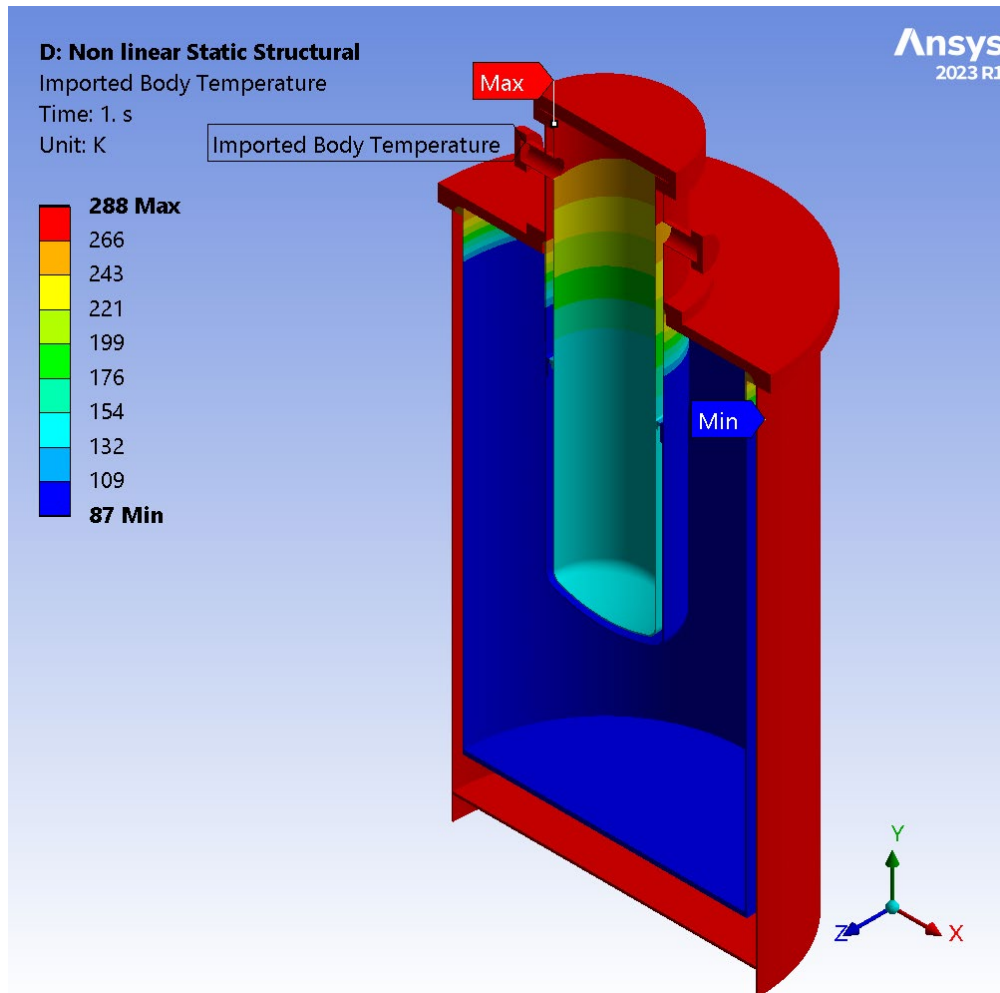

Figure 6-18: Imported temperature field in the Thermo-mechanical analysis

Other mechanical loads applied in the structural analysis (see **Figure 6-19**) are:

 ➢ A: Gravity, along the vertical axis of the cryogenic chamber: $g = 9.8066$ m/s^2.
 ➢ B: Pressure acting on the internal surfaces of the cryogenic chamber: $p_{int} = 100$ mbar.
 ➢ C: Pressure acting on the external surfaces of the cryogenic chamber: $p_{ext} = 1000$ mbar.

The bolt connections, with their pretension loads, and the roughness between the surfaces of the flanges in contact, were not implemented in the analysis: this is a precise choice to avoid this kind of non-linearity. So, the contact elements between the flanges were defined "bonded".
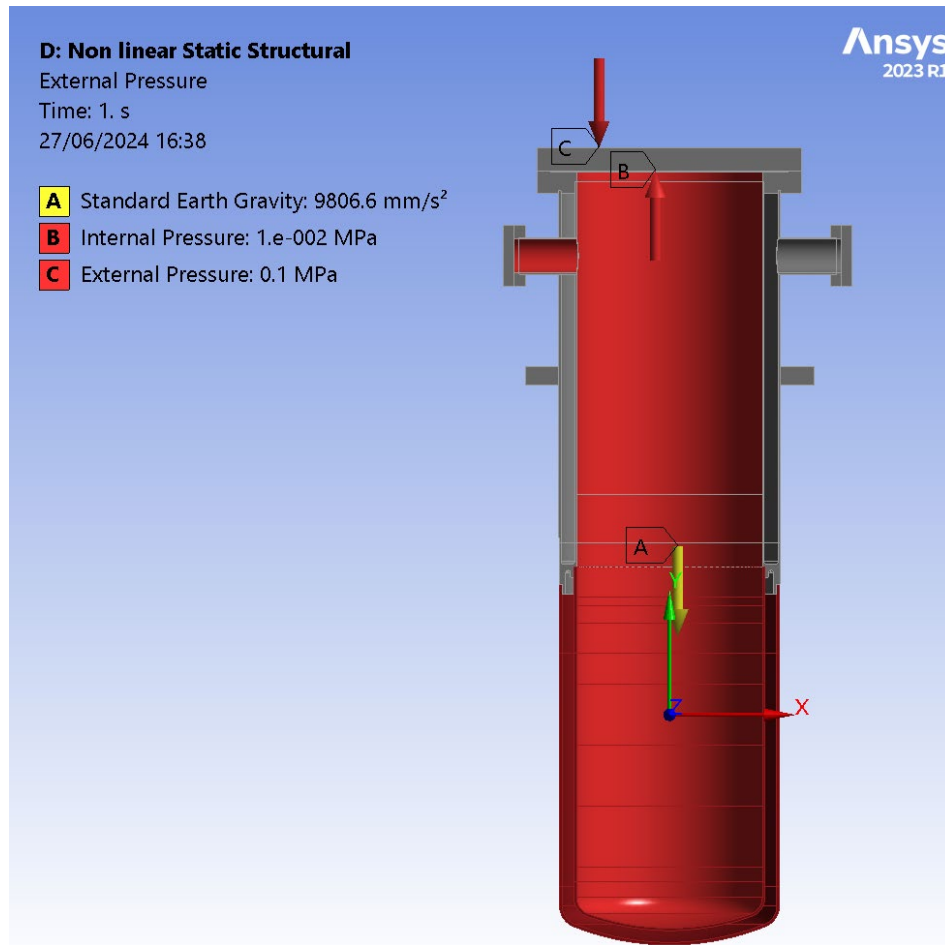
Figure 6-19: Mechanical loads of the Thermo-mechanical analysis

6.2.5 Safety conditions of the Thermo-mechanical analysis

The Thermo-mechanical analysis aims to verify the structural strength of the cryogenic chamber in operating condition, with a focus on the peaks of stress located in the thermal bridge region, where the effect of the CTE is more evident.

To perform this mechanical evaluation, it is necessary to define the admissible stresses for each material.

OFHC copper, **annealed**, has a Yield Stress $\sigma_{y,Cu} \cong$ **42 MPa** at T = 77 K, as it results from the cryogenic tensile test carried out on specimen #3 (this is the stress value related to a residual plastic deformation ε_p = 0.2%, conventionally assumed for ductile metals), after the first load/unload cycle, which should roughly reproduce the hardening state after the initial vacuum tests of the cryogenic chamber. It's known that the annealed copper undergoes hardening if stress reaches and exceeds the Yield Stress value and, consequently, it increases its mechanical strength in the following load cycle. So, it's reasonable to assume that, if the maximum Von Mises equivalent stress given by FEA reaches the Yield Stress value over a limited region close to the thermal bridge, this condition can lead to very small deformations to the copper chamber without any structural damage but, in the meantime, its mechanical strength increases. Under these assumptions, the copper Yield Stress can be considered the reference value of stress to evaluate the structural safety close to the SS bridge, considering that the UTS value is further higher by a factor 7.5.

For the other parts of the cryogenic chamber, made of **AISI 316L stainless steel**, the maximum Von Mises stress expected should be well below the Yield Stress related to the annealed metallurgical state, at the reference temperature of 293 K. It's known that the Yield stress value of AISI 316L increases going down to cryogenic temperatures so, it's reasonable to assume a safety factor 1.5 to define the maximum admissible stress:

$$\sigma_{adm,ss} = \frac{\sigma_{y,ss}}{Sf} = \frac{229.6}{1.5} = \mathbf{153\ MPa}\ \text{at T} = 293\ K$$

The operative life of the ASTAROTH apparatus foresees the realization of a limited number of cooling and heating cycles (3-4 cycle/year, ~ 20 in total), after which the cryogenic equipment will be decommissioned, so there are not fatigue issues to be evaluated with FEA.

However, another structural issue of the cryogenic chamber is the buckling, both under vacuum test at the environment temperature (+20°C), and under operating condition after the cooling down: it will be evaluated by a dedicated FEA (see **par. 6.3**).

The evaluation of the mechanical strength of the brazing between OFHC copper chamber and the thermal bridge made in AISI 316L was carried out by means of experimental tests described in **Section 5**.

6.2.6 *Thermo-mechanical FEA results*

Figure 6-20 shows the Total Deformation of the cryogenic chamber, in operating conditions, plotted with a deformation scale factor 10, against the undeformed wireframe.
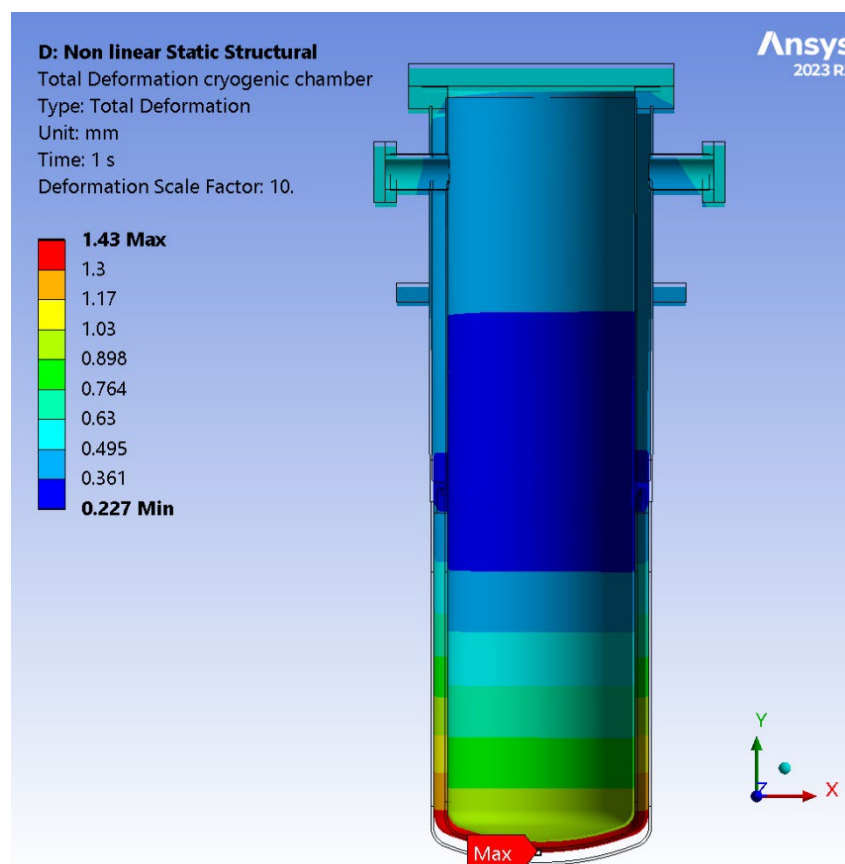

Figure 6-20: Total Deformation of the cryogenic chamber in operating condition

Figure 6-21 shows that the maximum Directional Deformation of the cryogenic chamber along the vertical Y axis is 1.5 mm, whereas the gap between the two bottom walls (internal and external) of the vacuum cavity is reduced by about 0.45 mm.
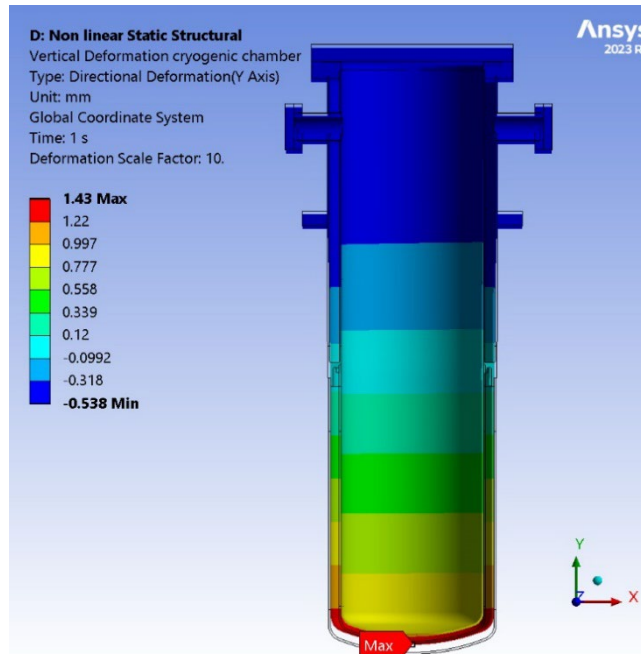

Figure 6-21:Vertical Deformation of the cryogenic chamber

Figure 6-22 shows the Radial Deformation of the cryogenic chamber, evaluated in a cylindrical coordinate system. The maximum Radial Deformation due to the shrinkage is -0.42 mm, and the gap between the two walls of the vacuum cavity is reduced less than 0.15 mm.
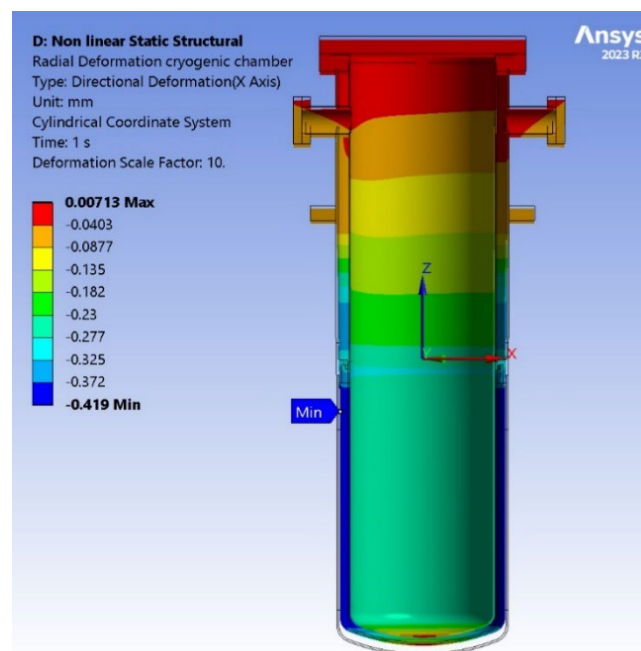
Figure 6-22: Radial Deformation of the cryogenic chamber

The Von Mises stress of the cryogenic chamber, resulting by FEA, is shown in **Figure 6-23,** which demonstrates that the peaks of stress are located on the thermal bridge.
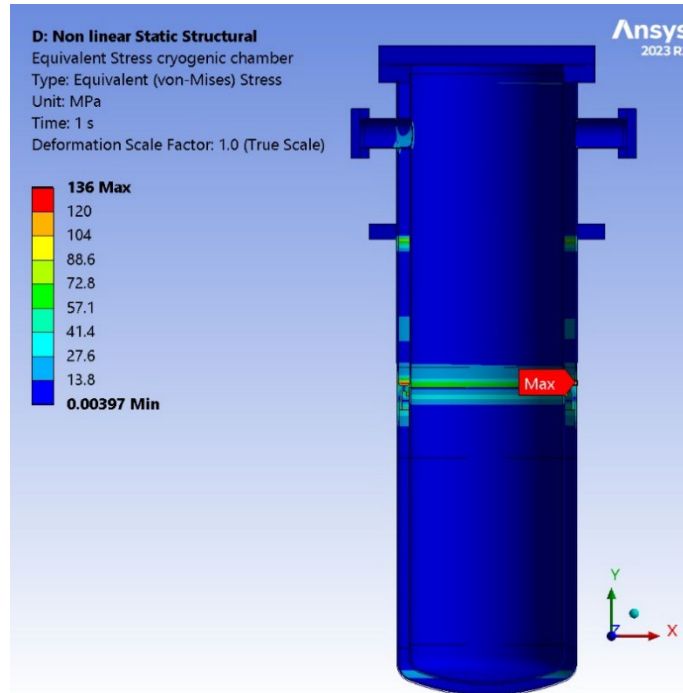

Figure 6-23: Von Mises stress of the cryogenic chamber

Over the AISI 316L bridge, the maximum Von Mises stress is reached on the radius of the outer wall (see **Figure 6-24**):

$$\sigma_{eq,SS,max} = 136\ MPa < \sigma_{adm} = 153\ MPa\ (@\ T = 293K)$$

which means the safety factor is greater than 1.5:

$$sf = \frac{\sigma_{y,SS}}{\sigma_{eq,max}} = \frac{229.6\ MPa}{136\ MPa} = 1.69$$
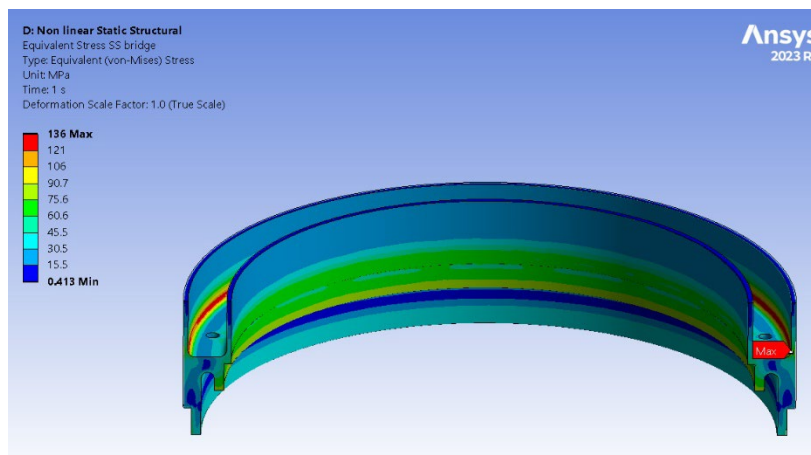

Figure 6-24: Von Mises stress of the AISI316L bridge

Before evaluating the stress of the copper chamber, it is useful to plot the Equivalent Plastic Strain, in order to visualize which regions, if any, are subjected to plastic deformation.

Figure 6-25 shows the Equivalent Plastic Strain of the external wall of the copper chamber, which involves the region in contact with the SS bridge, approximately 18 mm high starting from the upper edge.
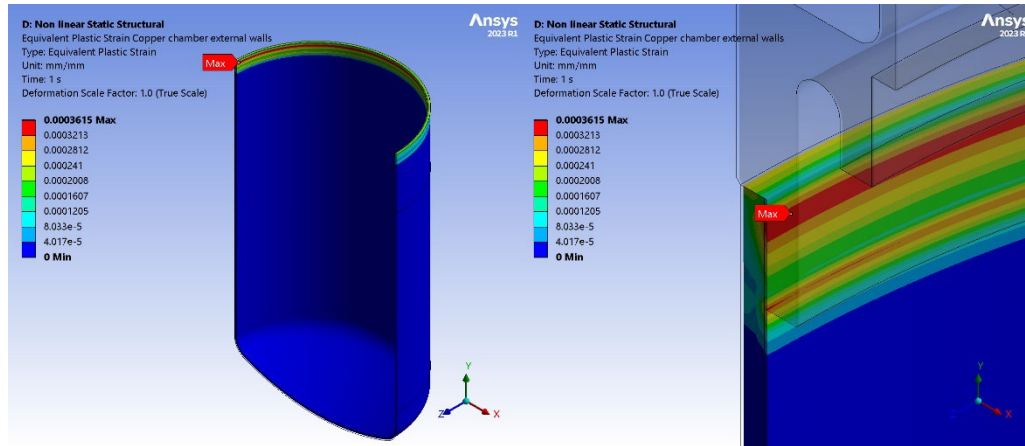

Figure 6-25: Equivalent Plastic Strain of the copper chamber external wall

Figure 6-26 shows the Von Mises stress of the external wall of the copper chamber. The region of the plastic deformation reaches a value of stress between 30 ÷ 37.9 MPa (red and orange contour plot).
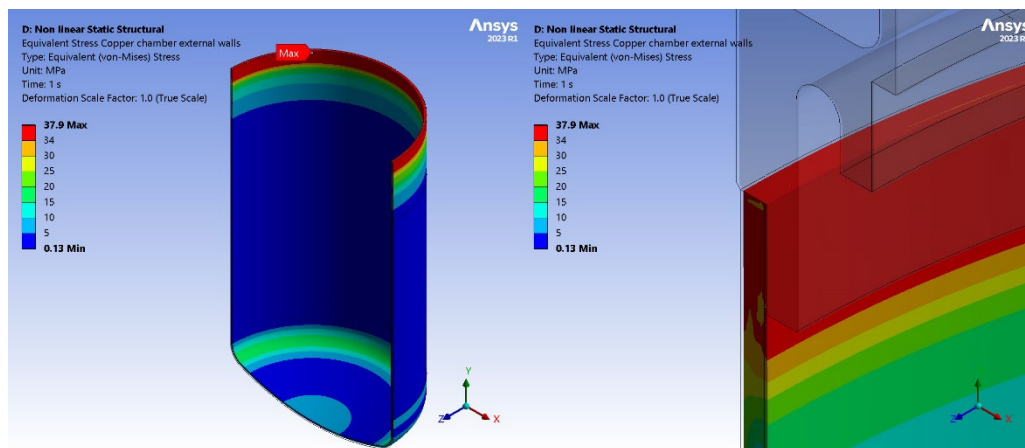

Figure 6-26: Von Mises stress of the copper chamber external wall

Being the overall temperature of the external wall of the copper chamber equal to 87 K (by thermal analysis) and assuming, in first approximation, the Yield stress of the OFHC copper at 87 K equal to $\sigma_{y,Cu,77K} = 42.3\ MPa$, measured at the temperature of 77 K:

$$\sigma_{eq,Cu,max} = 37.9\ MPa < \sigma_{y,Cu,77K} = 42.3\ MPa$$

With reference to the isotropic hardening curve of the annealed OFHC copper at 77 K (**Figure 6-14**), it is clear that the plastic deformation related to the maximum value of Von Mises stress $\sigma_{eq,Cu,max} = 37.9\ MPa$, is approximatively around 0.012% ÷ 0.032%, below the reference value of the Yield stress (0.2%). This fact means that, in operating condition, a very small plastic deformation occurs, which should lead to a local hardening so, it is very likely that the Chamber could work following a total linear elastic behavior in subsequent cooling cycles.

Figure 6-27 shows the equivalent plastic strain of the internal wall of the copper chamber, which is clearly located only on the contact region between the copper wall and the edge of the SS bridge, within 0.018%.
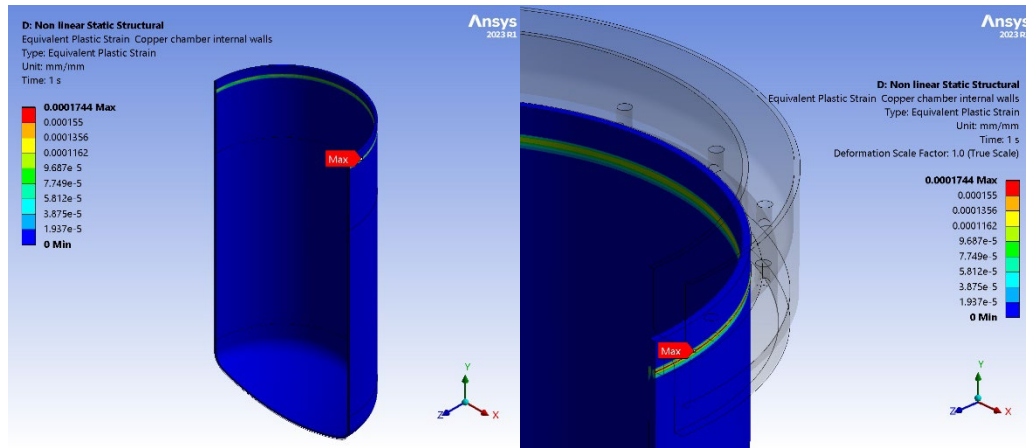

Figure 6-27: Equivalent Plastic Strain of the copper chamber internal wall

Figure 6-28 shows the Von Mises stress of the internal wall of the copper chamber. In the region of the plastic deformation the maximum value of Von Mises stress is between $30 \div 36.8$ MPa (red and orange contour plot).
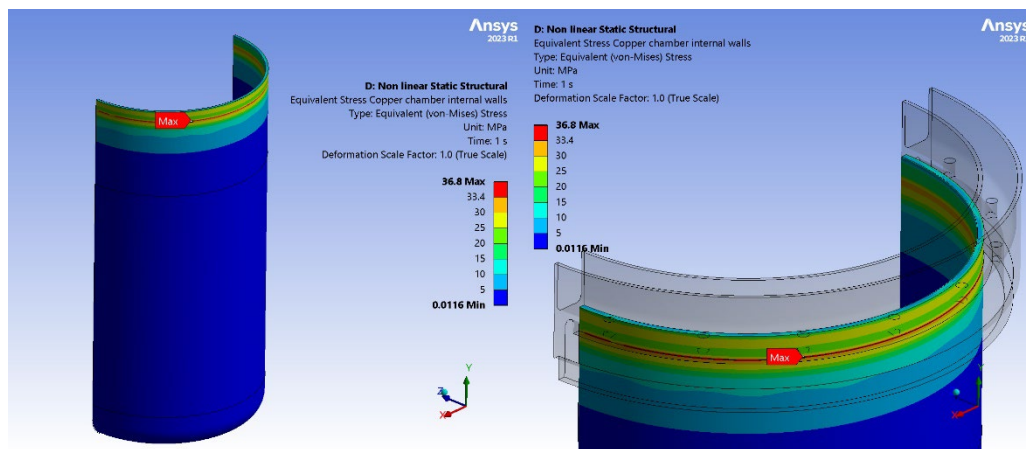

Figure 6-28: Von Mises stress of the copper chamber internal wall

The average temperature of the copper chamber internal wall is close to 145 K, so the Yield stress should be evaluated at this temperature. Assuming a linear variation of the Yield stress between the values known, which are $\sigma_{y,Cu,77K} = 42.3$ MPa at 77K and $\sigma_{y,Cu,293K} = 19.5$ MPa at 293.15 K, the value at 145 K can be estimated to be: $\sigma_{y,Cu,145K} \approx 35.2$ MPa.

So,

$$\sigma_{eq,Cu,max} = 36.8\ MPa > \sigma_{y,Cu,145K} = 35.2\ MPa$$

and a very localized hardening should occur, with a permanent deformation slightly greater than 0.2%. However, looking at the **Figure 6-27**, the maximum Equivalent Plastic Strain calculated by FEA is lower than 0.2%, being approximately 0.018%. This mismatch could be due to a FEA approximation calculating the stress gradient, being the region involved in the plastic deformation very small.

In conclusion, under operating conditions, the copper chamber works substantially within the linear elastic limits, except small regions in contact with the SS bridge. In these regions, a plastic deformation between 0.012%÷ 0.036% occurs (FEA results), and it should lead to a slight hardening, which could increase the Yield limit in the subsequent cooling cycles.

The maximum Von Mises stress is close to the Yield stress (≈ 38 MPa) but it is much lower than the UTS (320 MPa at 77 K), by at least a factor 8.

The FEA results show that, **in operating conditions**, the **cryogenic chamber can safely operate.** However, buckling stability should be verified: this is demonstrated in the next **par. 6.3**

6.3 Structural Stability Finite Element Analysis

The cryogenic chamber requires an evaluation of its structural stability, due to the fact that it is a dual-walled tank with vacuum in the cavity.
At the onset of an instability (buckling), any structure will develop a very large change in displacement, corresponding to essentially no change in load, beyond a small load perturbation. The existence of geometric imperfections can accelerate the buckling.
In general, below the so-called "critical load" a structure is in stable equilibrium: if a small perturbing force is introduced and then removed, the structure will return to its original position. Above the critical load the structure is in unstable equilibrium and any perturbing force will cause collapse. At the critical load the structure is in neutral equilibrium.
A real structure generally will become unstable at a load lower than the critical load because of imperfections and nonlinear behaviors.
A linear buckling analysis is based on a classic eigenvalue problem and uses the perturbation method; it must be preceded by a static structural analysis known as the pre-stress analysis, obtaining the stiffness state at a desired result set. Hence, for a linear buckling analysis, the eigenvalue problem is solved to get the **buckling load multiplier** (λ_i) and **buckling modes** (ψ_i): the buckling load conditions are computed by multiplying the applied loads by the buckling load factors.
At least one form of nonlinearity can be defined in the pre-stress static analysis: in our case, the **nonlinearity of the copper mechanical properties**.
In a **Nonlinear Based Eigenvalue Buckling analysis, load multipliers scale the loads applied in the buckling analysis only; therefore, when estimating the buckling load for the structure, it is necessary to account for the loading applied in both static structural and eigenvalue analyses:**

$$F_{BUCKLING} = F_{STATIC} + \lambda_i \cdot F_{PERTURBATION}$$

6.3.1 Buckling analysis of the cryogenic chamber: vacuum test at room temperature

This analysis reproduces the load case of the cryogenic chamber subjected to the vacuum test, carried out at room temperature (293.15 K): the vacuum is applied in the cavity between the double wall, with external and internal atmospheric pressure (1000 mbar = 0.1 MPa), as shown in **Figure 6-29**. The symmetry condition of the FEM model with respect to the radial-axial plane has been maintained. The bottom surface of the flange has been constrained along Y,Z axis of a cylindrical coordinate system [A] while, in radial direction, only few nodes laying on the vertical axis and, consequently on the symmetry plane, have been constrained [B], as shown in **Figure 6-30**.
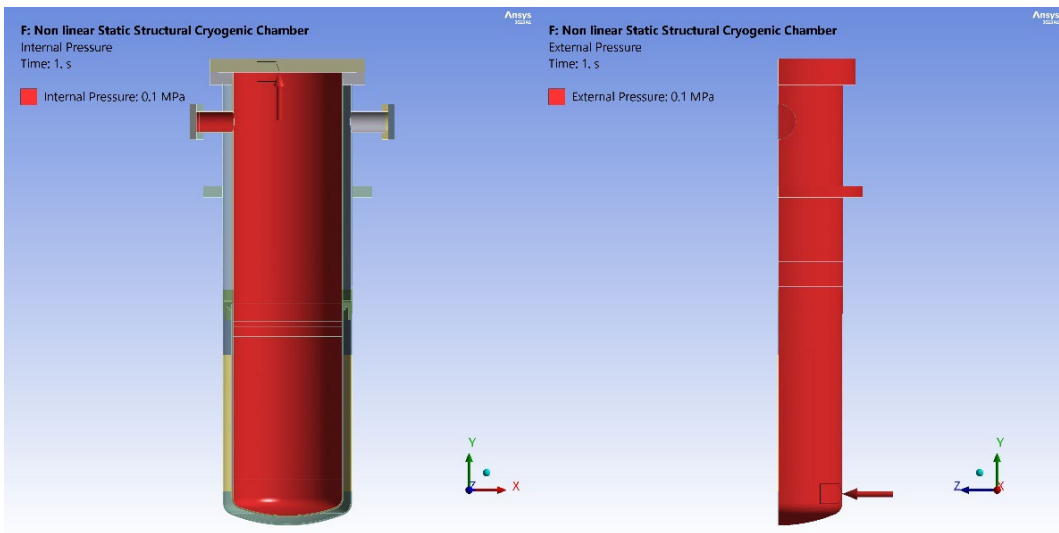Gravity has been applied as already shown in **Figure 6-19**.

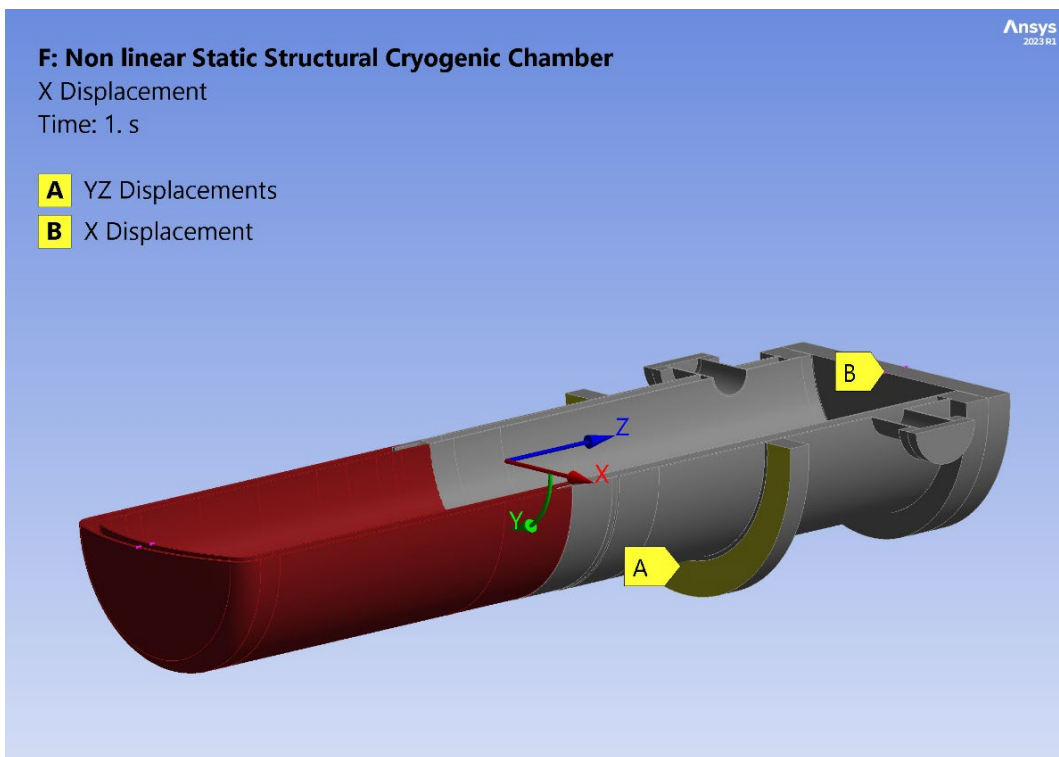**Figure 6-29: pressure loads during vacuum test of the cryogenic chamber**

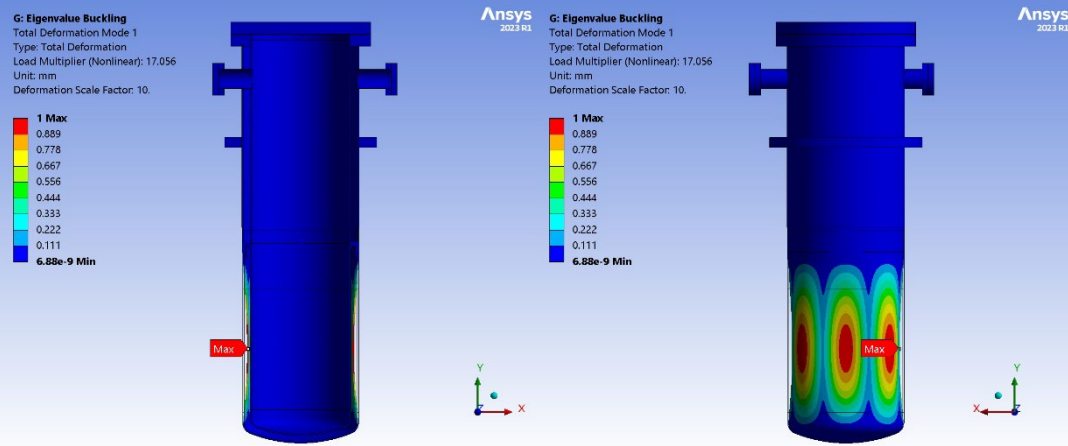**Figure 6-30: Constraints condition of the vacuum test buckling analysis**

Figure 6-31 shows the FEA result of the Nonlinear buckling analysis, which is the deformation of the first buckling mode (ψ_1) and its buckling load multiplier, $\lambda_1=17.056$.

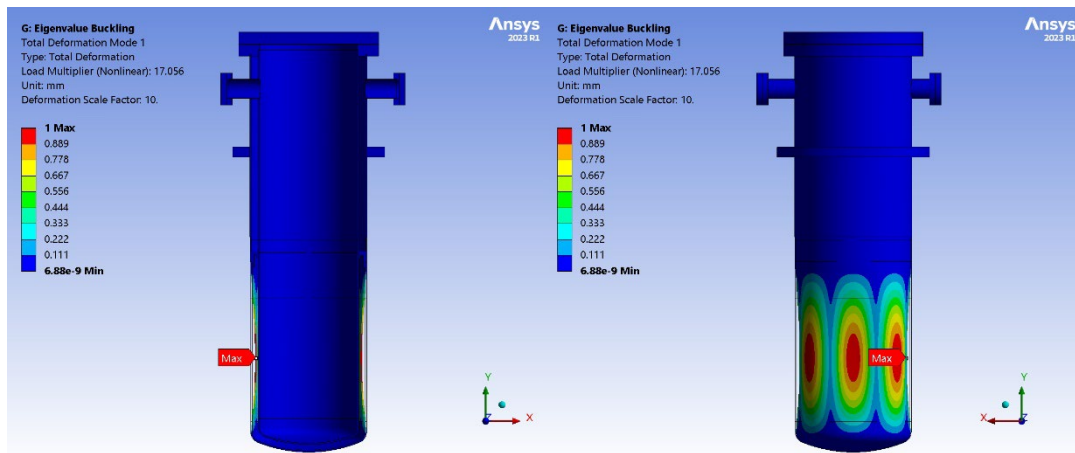The safety margin is large, even considering possible defects within manufacturing tolerances.

Figure 6-31: First buckling mode of the cryogenic chamber under vacuum test

6.3.2 *Buckling analysis of the cryogenic chamber: operating condition*

This analysis reproduces the cryogenic chamber loads and temperatures, in operating conditions. Temperatures of the metallic components are imported from the thermal analysis. The cavity between the two walls is always assumed to be under vacuum; the pressure acting on the external surfaces of the cryogenic chamber, inside the dewar, is conservatively taken as 1500 mbar (0,15 MPa), which is the highest operating value of the dewar. Outside the dewar there is the atmospheric pressure (1000 mbar = 0.1 MPa). Helium gas low pressure, 100 mbar (0.01 MPa), is applied on the inner walls of the cryogenic chamber. The pressure loads applied in the FEA are shown in **Figure 6-32**.
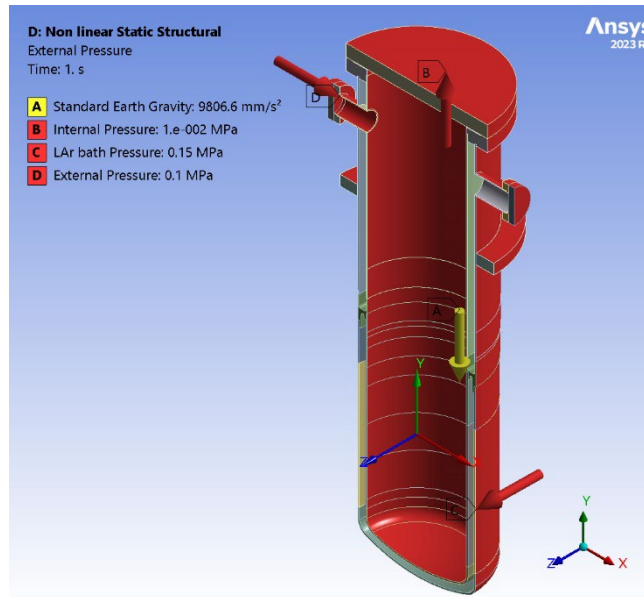
Figure 6-32: pressure loads on the cryogenic chamber in operating condition

The constraints conditions of this analysis are the same of the Thermo-mechanical FEA already described in **par. 6.2.3** and shown in **Figure 6-17**.

Figure 6-33 shows the FEA result of the Nonlinear buckling analysis, which is the deformation of the first buckling mode (ψ_1) and its buckling load multiplier, $\lambda_1 =$**23.962**.

Under operating conditions, the buckling safety margin is greater than the value obtained by the FEA of the vacuum test of the cryogenic chamber at room temperature.
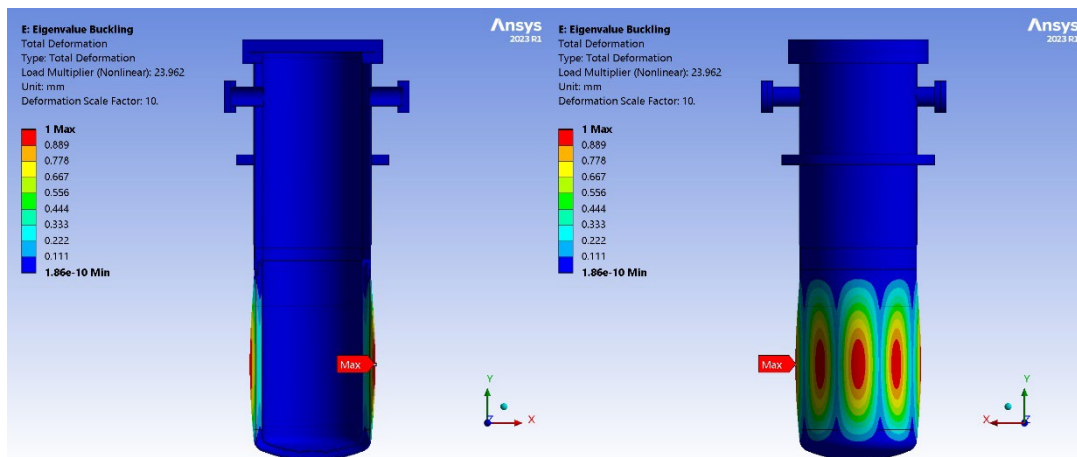

Figure 6-33: First buckling mode of the cryogenic chamber in operating condition

In both load cases (vacuum test and operating condition) the failure occurs on the external cylindrical wall of the copper chamber, with different deformation shapes (**Figure 6-34**). The load multiplier is lower under the vacuum test condition, but large enough to guarantee the structural stability.
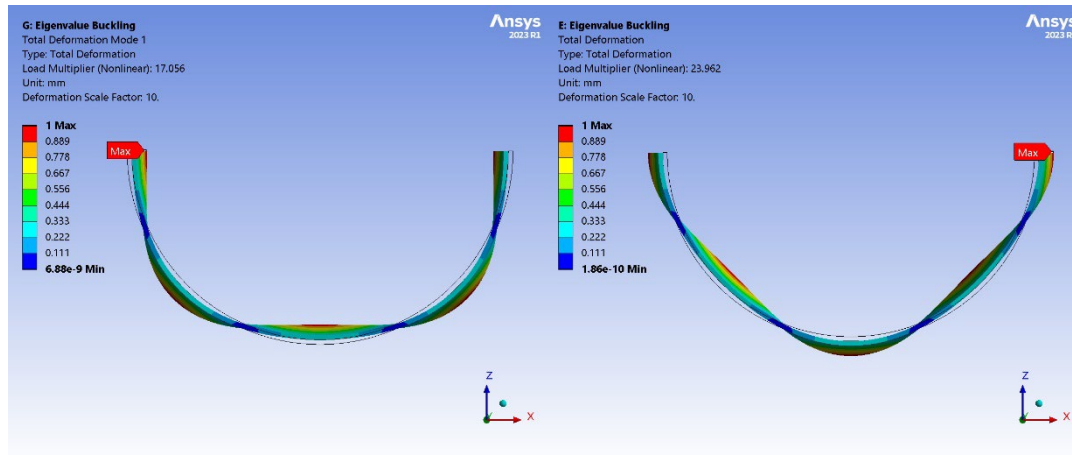
Figure 6-34: deformation of the outer copper wall of the cryogenic chamber, due to the first buckling mode, under vacuum test at room temperature (left) and operating condition (right).

7   Conclusions

This technical note introduces the cryogenic chamber of the ASTAROTH project, an R&D INFN program meant to develop the next generation of detectors based on NaI(Tl) crystals for the detection of Dark Matter.

The note is dedicated to the thermo-mechanical simulation of the cryogenic chamber, developed at INFN Milano to demonstrate the robustness of the design and its reliability for the use in the R&D program that is carried out at INFN LASA Laboratory - Segrate (MI).

The collaboration soon realised that the data in literature concerning in particular the copper were not sufficient to gather the correct set of inputs for the simulation. Therefore, it was realised that dedicated tensile and bending tests were needed, on the very same material used for the chamber, in order to constrain the necessary mechanical properties to feed into the simulation.

Section 4 is then dedicated to the thorough description of the tensile tests performed, at room temperature and at 77 K, on two sets of copper samples, at INFN LASA. The tests allowed deriving values for Young Modulus, Yield Stress and UTS, to be later fed into the simulation.

Section 5 instead concentrates on bending tests on samples of a brazed connection between copper and stainless steel: indeed, the information about the cryogenic behaviour of the brazing paste was not available in literature, as well. The bending tests were successful in demonstrating the reliability of the brazed connection in the stress range that the chamber will undergo.

Section 6 is the main focus of this note and details the FEA performed with the ANSYS software. In the following, the main results of the simulations are summarised.

7.1   Thermal FEA

A dissipated power of 180 W, in opposition to the LAr bath at 87 K, is adequate to obtain a uniform temperature below 150 K inside the cryogenic chamber volume (the first thermal requirement), and to obtain a uniform temperature of the crystals within 0.1 K (the second thermal requirement).

7.2   Thermo-mechanical FEA of the cryogenic chamber in operating condition

Vertical and radial deformation are within expected limits and don't create any issue to the vacuum cavity of the copper chamber.

For the parts made of AISI 316L, the maximum Von Mises stress is reached on the radius of the bridge, and its value is below the maximum admissible stress, with a safety factor of 1.69.

The copper chamber works substantially within the linear elastic limits, except small regions in contact with the SS bridge. In these regions a plastic deformation between $0.012\% \div 0.036\%$ occurs, and it should lead to a slight hardening. Here, the maximum Von Mises stress is close to the Yield stress (≈ 38 MPa) but it is much lower than the UTS (320 MPa at 77 K), by at least a factor 8.

7.3 Nonlinear buckling FEA

The most critical load condition, for buckling, is the vacuum test at room temperature, since the mechanical properties of the OFHC copper annealed at 293.15 K are significantly lower than those at cryogenic temperature. The resulting minimum buckling load multiplier ($\lambda_1 = 17.056$) guarantees a large safety margin, even considering possible defects within the manufacturing tolerances limits.

In conclusion, **all the FEA simulations performed confirm the robustness of the cryogenic chamber design, which meets all the thermal requirements and ensures that it can operate safely under operating conditions**.

8   Acknowledgements

Bibliography

1. Bernabei R. et al. [DAMA Collaboration], Eur Phys J C73, 2648 (2013)

2. XENON Collaboration, JINST 18, P07054 (2023)

3. P. Agnes et al. [DarkSide Collaboration], Phys. Rev. D 98, 102006 (2018)

4. A. H. Abdelhameed et al. [CRESST Collaboration], Phys. Rev. D 100 102002 (2019)

5. F. Calaprice et al., Eur Phys J C82(12), 1158 (2022)

6. G. Adhikari et al. [COSINE-100 Collaboration], Phys. Rev. D 106, 052005 (2022)

7. J. Amaré et al., Phys. Rev. D 103, 102005 (2021)

8. D. D'Angelo et al., The ASTAROTH Project, AIP Conf. Proc. 2908, 100007 (2023)

9. D. D'Angelo, Riunione di Commissione V, 10-11 Febbraio2020, Presidenza INFN – Roma
   https://agenda.infn.it/event/21625/contributions/109659/attachments/70454/87907/astaroth_csn5_feb2020_v2.pdf

10. www.lsndiffusion.com, paste LSNi-2 MSDS